

# A successful search for intervening 21 cm HI absorption in galaxies at $0.4 < z < 1.0$ with the Australian Square Kilometre Array Pathfinder (ASKAP)

Elaine M. Sadler<sup>1,2,3\*</sup>, Vanessa A. Moss<sup>2,4</sup>, James R. Allison<sup>5,3</sup>, Elizabeth K. Mahony<sup>2</sup>, Matthew T. Whiting<sup>2</sup>, Helen M. Johnston<sup>1</sup>, Sara L. Ellison<sup>6</sup>, Claudia del P. Lagos<sup>7,3</sup>, Bärbel S. Koribalski<sup>2</sup>

<sup>1</sup>*Sydney Institute for Astronomy, School of Physics, University of Sydney, NSW 2006, Australia*

<sup>2</sup>*ATNF, CSIRO Astronomy and Space Science, PO Box 76, Epping, NSW 1710, Australia*

<sup>3</sup>*ARC Centre of Excellence for All Sky Astrophysics in 3 Dimensions (ASTRO 3D)*

<sup>4</sup>*ASTRON, The Netherlands Institute for Radio Astronomy, Postbus 2, NL-7900 AA Dwingeloo, the Netherlands*

<sup>5</sup>*Sub-Dept. of Astrophysics, Department of Physics, University of Oxford, Denys Wilkinson Building, Keble Rd., Oxford, OX1 3RH, UK*

<sup>6</sup>*Department of Physics & Astronomy, University of Victoria, Finnerty Road, Victoria, British Columbia V8P 1A1, Canada*

<sup>7</sup>*International Centre for Radio Astronomy Research, The University of Western Australia, Crawley, WA 6009, Australia*

Accepted XXX. Received YYY; in original form ZZZ

## ABSTRACT

We have used the Australian Square Kilometre Array Pathfinder (ASKAP) radio telescope to search for intervening 21 cm neutral hydrogen (HI) absorption along the line of sight to 53 bright radio continuum sources. Our observations are sensitive to HI column densities typical of Damped Lyman Alpha absorbers (DLAs) in cool gas with an HI spin temperature below about 300–500 K. The six-dish Boolardy Engineering Test Array (BETA) and twelve-antenna Early Science array (ASKAP-12) covered a frequency range corresponding to redshift  $0.4 < z < 1.0$  and  $0.37 < z < 0.77$  respectively for the HI line. Fifty of the 53 radio sources observed have reliable optical redshifts, giving a total redshift path  $\Delta z = 21.37$ . This was a spectroscopically untargeted survey, with no prior assumptions about the location of the lines in redshift space. Four intervening HI lines were detected, two of them new. In each case, the estimated HI column density lies above the DLA limit for HI spin temperatures above 50–80 K, and we estimate a DLA number density at redshift  $z \sim 0.6$  of  $n(z) = 0.19^{+0.15}_{-0.09}$ . This value lies somewhat above the general trend of  $n(z)$  with redshift seen in optical DLA studies. Although the current sample is small, it represents an important proof of concept for the much larger 21 cm *First Large Absorption Survey in HI* (FLASH) project to be carried out with the full 36-antenna ASKAP telescope, probing a total redshift path  $\Delta z \sim 50,000$ .

**Key words:** galaxies: ISM – galaxies: evolution – (galaxies:) quasars: absorption lines – radio lines: ISM – radio continuum: general – instrumentation: interferometers

## 1 INTRODUCTION

### 1.1 Neutral hydrogen in the distant Universe

Almost all our current knowledge about the amount and distribution of neutral hydrogen (HI) beyond the local (redshift  $z \lesssim 0.2$ ) Universe comes from optical studies of QSO

absorption lines. The strongest of these lines, the Damped Lyman- $\alpha$  Absorbers (DLAs), arise in sight-lines with HI column densities above  $2 \times 10^{20}$  atoms  $\text{cm}^{-2}$ , i.e. similar to the typical column density in the Milky Way disk (Wolfe et al. 1986, 2005). DLAs are thought to account for the bulk of the cosmic HI mass density across a wide range in redshift, and so are important tracers of the neutral-gas reservoirs for star formation in the distant Universe.

\* E-mail: elaine.sadler@sydney.edu.au

Large optical QSO surveys for DLAs are only possible

at redshift  $z \gtrsim 1.7$ , where the ultraviolet Ly $\alpha$  absorption line is redshifted to wavelengths visible with ground-based telescopes. At lower redshifts the Mg II absorption line has been used to select candidate DLA systems (Briggs & Wolfe 1983; Rao & Turnshek 2000; Rao et al. 2006; Ellison 2006; Kanekar et al. 2009; Rao et al. 2017), but follow-up ultraviolet spectroscopy with the *Hubble Space Telescope* (*HST*) is then needed to measure the Ly $\alpha$  line profile and HI column density so the samples studied are much smaller. In addition, it is not straightforward to understand and quantify the selection biases present in these pre-selected samples and this can introduce further uncertainties in estimates of the cosmic HI mass density at  $z < 1.7$  (Rao et al. 2006; Neeleman et al. 2016; Rao et al. 2017; Berg et al. 2017).

Other approaches have been used to probe HI in the redshift range  $0.2 \lesssim z \lesssim 1.7$ , including HI emission-line stacking (Lah et al. 2007; Delhaize et al. 2013; Kanekar et al. 2016) and measurements of the UV spectra of QSOs observed with the Hubble Space Telescope without any MgII preselection (Neeleman et al. 2016), but the amount and distribution of HI in galaxies in this redshift range remains poorly constrained.

The extent to which optical DLA surveys are affected by dust obscuration remains unclear. Absorbers with a high HI column density may contain enough dust to redden and dim the light of background QSOs so that they are missed by colour-selected, flux-limited samples (Fall & Pei 1989). A study of radio-selected QSOs by Ellison et al. (2005) suggests that the effect is generally small, with only a modest increase in reddening for typical absorbers (mean  $E(B - V) < 0.04$  mag), though individual DLA systems with much higher reddening have also been identified (Heintz et al. 2018; Geier et al. 2019). Pontzen & Pettini (2009) estimate that around 7 percent of DLAs at redshift  $1.8 < z < 3.5$  are missing from optical samples due to dust obscuration, while Krogager et al. (2019) suggest that optical DLA studies underestimate the cosmic mass density of neutral hydrogen by 10–50 percent at  $z \sim 3$ , and by up to a factor of two at  $z = 2.2$ . Previous studies have concentrated mainly on ground-based surveys for DLAs at  $z > 1.7$ , and the effects of dust obscuration in lower-redshift DLA systems at  $z < 1$  remain to be quantified.

In principle, radio measurements of the 21 cm HI absorption line provide an alternative tool for identifying DLA systems, particularly at redshift  $z < 1.7$  where ground-based optical DLA studies are not possible (e.g. Kanekar & Briggs 2004; Morganti et al. 2015). Importantly, because the optical depth of the 21-cm absorption line is inversely related to its excitation (spin) temperature, it is most sensitive to the cold neutral medium (CNM;  $T \sim 100$  K). This is the component of the HI most likely to trace star formation in galaxies and therefore directly follow its evolution throughout cosmic history (see e.g. Kanekar et al. 2014 and references therein). Since 21 cm HI absorption measurements in the radio are unaffected by dust obscuration along the line of sight, they may also help clarify the extent to which optical DLA studies have been affected by a dust bias.

A handful of 21 cm DLAs have been detected in blind<sup>1</sup> searches with single-dish radio telescopes (Brown & Roberts

1973; Brown & Mitchell 1983; Darling et al. 2004), but these searches were limited both by the available spectral bandpass and by the effects of terrestrial radio interference (e.g. Hunt et al. 2016). As noted by Wolfe et al. (2005), the redshift interval covered by a single optical spectrum,  $\Delta z \sim 1$ , is large compared to that sampled by early radio 21 cm surveys (typically  $\Delta z \sim 0.02$ ) so that optical surveys were more efficient at covering a large redshift path length. These earlier limitations have now largely been removed through (i) the advent of new wide-band correlators for radio interferometers that provide instantaneous redshift coverage approaching that of optical spectrographs, and (ii) the construction of new SKA pathfinder and precursor radio telescopes on radio-quiet sites.

In this paper, we present the results from a blind 21 cm search towards 53 bright radio sources for HI absorption in galaxies at redshift  $0.4 < z < 1.0$ . The observations were carried out in commissioning time with the first 6–12 dishes of the Australian SKA Pathfinder (ASKAP) telescope (McConnell et al. 2016). This work is intended to pave the way for a blind, all-sky 21 cm absorption survey, the First Large Absorption Survey in HI (FLASH) to be carried out with the full 36-dish ASKAP telescope. Recent early science results from FLASH have discovered an intervening 21-cm absorber in the 50-square-degree GAMA 23 field, demonstrating the feasibility of such a wide-field survey (Allison et al. 2020). However, FLASH has not yet covered enough sky area to return a high detection yield. By targeting a modest sample of very bright radio sources, we aim here to provide the first constraint of the number density of 21-cm absorbers at intermediate cosmological redshifts.

Throughout this paper we adopt the cosmological parameters  $H_0 = 70$  km s<sup>-1</sup> Mpc<sup>-1</sup>,  $\Omega_\Lambda = 0.7$  and  $\Omega_m = 0.3$ .

## 1.2 ASKAP and BETA

ASKAP (DeBoer et al. 2009) is a wide-field aperture synthesis radio telescope that uses novel phased array feed technology (PAF) to provide a 30 deg<sup>2</sup> field of view. The telescope is located at the radio-quiet Murchison Radio Observatory in Western Australia, and works in the frequency range 700–1800 MHz. The full array of 36 × 12 m ASKAP dishes came into operation in early 2019.

The Boolardy Engineering Test Array (BETA; Hotan et al. 2014; McConnell et al. 2016) connected six ASKAP dishes equipped with first-generation (MkI) PAFs and operated from March 2014 to February 2016. Although BETA was originally intended purely as an engineering and commissioning testbed, some early science observations were also carried out (e.g. Allison et al. 2015; Serra et al. 2015; Heywood et al. 2016). The longest baseline for the BETA array was 916 m, giving an angular resolution of about 1.8 arcmin at 850 MHz. The frequency resolution was 18.5 kHz, corresponding to a rest-frame velocity resolution of  $\sim 6$  km s<sup>-1</sup>.

In early observations with BETA, Allison et al. (2015) detected 21 cm HI absorption at  $z = 0.44$  against a bright radio continuum source, PKS 1740-517, whose spectroscopic

untargeted and uses no prior assumptions about the redshift of any HI absorption lines

<sup>1</sup> By a ‘blind’ search, we mean a search that is spectroscopically

redshift was unknown at the time. They found that the spectral dynamic range achievable with BETA was excellent for carrying out a blind absorption survey, and that the lowest ASKAP frequency band (covering 700-1000 MHz), where the MkI PAFs were most sensitive, was essentially free of terrestrial radio-frequency interference (RFI). In spite of its limited collecting area, BETA therefore proved to be an excellent instrument with which to search for new HI absorption lines in the redshift range  $0.4 < z < 1.0$  using bright ( $> 1$  Jy) continuum sources as probes (see e.g. Moss et al. 2017; Glowacki et al. 2019).

The data presented in this paper were observed either with BETA, or during commissioning time with a 12-antenna ASKAP Early Science array (ASKAP-12) in early 2017. The ASKAP-12 array was equipped with the second-generation MkII PAF receivers (Chippendale et al. 2015). ASKAP-12 provided higher sensitivity than BETA, but with a more limited frequency coverage at this early stage (799–1039 MHz, corresponding to  $0.365 < z < 0.775$  for HI – the 18.5 kHz frequency resolution remained unchanged). The longest baseline for the ASKAP-12 array was around 2.3 km, and the restoring beam for our data was  $\approx 50 \times 25$  arcsec (using Briggs’ robust weighting = 0.5).

### 1.3 What do we expect to see?

Two kinds of 21 cm absorption-line detections are possible: *associated* lines, where the neutral gas producing the absorption is within (or associated with) the radio source itself, and *intervening* lines, where the gas lies in a different galaxy somewhere along the line of sight to the radio source. Associated absorption lines (like the one seen in PKS 1740-517 by Allison et al. 2015) provide insights into the role of cold gas in AGN fuelling and feedback (see Morganti & Oosterloo 2018 for a recent review).

The focus of this paper is on intervening 21 cm absorption lines, which have the potential to provide an independent probe of the cosmic HI mass density and its evolution. Rao et al. (2017) estimate the probability of intercepting a Damped Lyman- $\alpha$  Absorber (DLA) with HI column density  $N_{\text{HI}} \geq 2 \times 10^{20} \text{ cm}^{-2}$  as:

$$n(z) = 0.027 \pm 0.007 (1+z)^{1.682 \pm 0.200}. \quad (1)$$

From this, we would expect  $\sim 5\%$  of sightlines with  $0.4 < z < 1.0$  (the HI redshift range spanned by the lowest-frequency ASKAP band at 700-1000 MHz) to intersect an intervening DLA with an HI column density above this limit.

How strong will these lines be? The observed HI 21 cm optical depth ( $\tau$ ) is related to the HI column density ( $N_{\text{HI}}$ ) by:

$$N_{\text{HI}} = 1.823 \times 10^{18} T_s \int \tau \Delta V, \quad (2)$$

where  $T_s$  (in K) is the harmonic mean spin temperature of the HI gas and  $\Delta V$  the total absorption-line width in  $\text{km s}^{-1}$ . The optical depth of the absorber can be estimated from the observed spectrum, but also depends on the areal fraction of the radio source covered by the absorber (the covering factor  $f$ ). If unknown, a fiducial value of  $f = 1$  is often used, which is equivalent to estimating the optical depth, and hence  $N_{\text{HI}}$ , as an average across the unresolved source.

Although 21 cm absorption-line measurements are particularly sensitive to colder gas, they do not provide a direct measurement of  $N_{\text{HI}}$  unless  $T_s$  is known or can be estimated. The spin temperature in Equation 2 is a column-density-weighted harmonic mean over all line-of-sight components of HI in the absorber. In the Milky Way ISM, the harmonic mean spin temperature is  $T_s \approx 300$  K, with three HI phases in pressure equilibrium, consisting of cold (CNM;  $T_s \approx 100$  K), unstable (UNM;  $T_s \approx 500$  K) and warm neutral medium (WNM;  $T_s \approx 10^4$  K), in mass fractions of 28, 20, and 52 per cent, respectively (Murray et al. 2018). In general we expect that the mass fractions of these phases will vary depending on the physical conditions within each absorber. Cooling of the HI is driven by fine structure emission lines of C II and O I, while heating occurs via the absorption of UV radiation by dust grains and subsequent photoelectric effect. The inferred spin temperature in a given 21-cm absorber is therefore dependent on the gas-phase metallicity, dust abundance and background UV field, and so likely to trace the evolutionary history of the galaxy.

There are very few measurements of HI spin temperature available for neutral gas in the redshift range  $0.4 < z < 1$ . Ellison et al. (2012) measured a spin temperature of  $90 \pm 23$  K at  $z=0.6$  for an intervening line against the  $z=1.25$  radio QSO J1431+3952, and Zwaan et al. (2015) derived a slightly lower value of  $64 \pm 17$  K for the same system. Kanekar et al. (2014) measured a range of spin temperatures from 90 K to  $> 1380$  K (median value  $\sim 270$  K) for eight DLA systems in the redshift range  $0.4 < z < 1$ . Where specific measurements are unavailable, many authors assume a fiducial spin temperature of 100 K, which equivalently corresponds to assuming that all of the absorbing gas is CNM. Using this value therefore gives a lower limit to the true column density of HI.

In the absence of detailed spin temperature measurements, Braun (2012) found a tight but strongly nonlinear relation between 21 cm absorption opacity and HI column density in Local Group galaxies at  $z = 0$ , and suggested that this relation might also be applicable at higher redshift. For a DLA system with  $N_{\text{HI}} \sim 2 \times 10^{20} \text{ cm}^{-2}$ , the Braun (2012) relation gives a typical observed peak opacity of  $\tau \sim 0.015$ .

To probe DLA-like HI column densities in gas clouds with HI spin temperatures typical of galaxy disks, we ideally need to be able to detect 21 cm absorption lines with a peak optical depth of  $\tau \sim 0.01 - 0.02$ . To make reliable detections, we also require excellent spectral dynamic range across the telescope’s bandwidth.

### 1.4 The expected locations of DLA systems at $0.4 < z < 1$

Information on the host galaxies of  $z < 1.7$  DLA systems is relatively sparse (Wolfe et al. 2005). Chen & Lanzetta (2003) found that the galaxies that give rise to DLA systems at  $z \leq 1$  span a wide range of morphological types, and that some DLAs may be associated with galaxy groups rather than individual galaxies.

On the theory side, simulations have presented contradictory results about where most of the HI is located, i.e. the relative contributions from the interstellar medium (ISM) of galaxies, the circum-galactic medium (CGM) and intergalactic gas as a function of cosmic time. van de Voort et al. (2012)

showed that in the OWLS hydrodynamical simulations, the CGM starts to dominate the HI density at  $z \gtrsim 1.5 - 2$ , but other cosmological hydrodynamical simulations, find that the ISM HI continues to dominate the cosmic abundance out to higher redshift (Davé et al. 2013). In Illustris-TNG, Diemer et al. (2019) showed that the CGM becomes an important contributor of neutral hydrogen at  $z \gtrsim 1$ . On the other hand, a comparison of cosmological semi-analytic models of galaxy formation (which only account for HI in the ISM of galaxies) with inferred measurements of  $\Omega_{\text{HI}}$  has been used to argue that the CGM may already be important at  $z \approx 1$  (Lagos et al. 2014, 2018).

The fact that some observations at intermediate redshifts,  $0.3 \lesssim z \lesssim 1$ , show DLAs to be associated with groups rather than individual galaxies (Péroux et al. 2019; Chen et al. 2019) may indicate that the CGM is a significant reservoir of HI at these redshifts, in contrast to the local ( $z \sim 0$ ) Universe where most of the HI is observed to be in the ISM of galaxies. Given these current uncertainties, new observational constraints are likely to play a vital role in distinguishing between the various models.

## 2 SAMPLE SELECTION

For ease of interpretation in this pilot study, we aimed to select background radio sources that were both bright and reasonably compact (i.e. had one or more radio components that were unresolved on arcsec scales).

We used the Australia Telescope 20 GHz (AT20G) Bright Source Sample (BSS) catalogue (Massardi et al. 2008) as the basis for our initial BETA target selection, since it contains a high fraction of radio-loud QSOs (with a median redshift of  $z \sim 1.2$ ) and so is dominated by distant, compact radio sources. This catalogue covers the whole sky south of declination  $-15^\circ$  (apart from a small strip with Galactic latitude  $|b| < 1.5^\circ$ ). For our later observations with ASKAP-12, we supplemented the BSS catalogue with more northerly objects from the main AT20G source catalogue (Murphy et al. 2010).

### 2.1 Target selection for BETA

We selected the initial pilot sample of bright radio continuum sources to observe with BETA based on two main considerations:

(i) The limited sensitivity of the BETA telescope means that the background radio sources used as probes need to be bright enough (ideally with flux density  $> 2$  Jy at 700–1000 MHz) to allow us to measure lines with optical depth  $\tau \sim 0.01$ , and to distinguish weak absorption lines from noise fluctuations in a reliable way.

(ii) The background sources should ideally be at redshift  $z > 1$  to allow us to probe the full  $\Delta z = 0.6$  redshift path length available with BETA, but we also included bright radio sources for which no optical redshift is currently available since these may be objects where a dusty galaxy intervenes along the line of sight to a distant radio source.

We began by selecting the 130 AT20G BSS objects with 20 GHz flux density above 1.0 Jy (38 of these have 20 GHz flux densities above 2.0 Jy), and removed Galactic sources

and other objects known to have redshift  $z < 0.4$ . This left 112 AT20G BSS sources. We then further restricted the list to objects with an NVSS or SUMSS flux density above 2.0 Jy (to ensure good S/N with BETA).

This left us with the final sample of 32 sources listed in Table 1. Two of these objects lack a reliable optical redshift. Of the remaining 30 sources, 17 are background sources for the whole ASKAP band (i.e. have redshift  $z > 1$ ) and 13 have redshifts that place the HI line within the lowest ASKAP band ( $0.4 < z < 1.0$ ). For the 13 ‘in-band’ radio sources with redshift  $z \leq 1.0$ , we reduced the assumed redshift path by  $\Delta z = 0.01$  to exclude the region within  $3000 \text{ km s}^{-1}$  of the emission redshift that may be occupied by associated HI absorption systems. After accounting for this ‘proximity effect’, the total redshift interval probed for intervening DLA systems by the 30 sources of known redshift is  $\Delta z = 14.00$ .

### 2.2 Target selection for ASKAP-12

We selected some additional bright, compact sources to observe with ASKAP-12 during commissioning time in February 2017. The improved sensitivity of this 12-antenna array allowed us to relax some of the constraints on our earlier BETA sample, and the new sources were chosen from the AT20G catalogue (Murphy et al. 2010) as follows:

(i) We relaxed the  $-15^\circ$  declination limit applied for the BETA sample, and included sources up to dec  $0^\circ$ .

(ii) As before, we excluded Galactic sources and other objects known to have redshift  $z < 0.4$ .

(iii) We include all the remaining objects with 20 GHz flux density above 0.5 Jy (rather than 1.0 Jy for the BETA sample) and NVSS or SUMSS flux density above 1.5 Jy (rather than 2.0 Jy for the BETA sample).

This left us with the sample of 21 additional sources listed in Table 2. Twenty of these objects have a reliable optical redshift, 18 are background sources for the whole ASKAP band (i.e. have redshift  $z > 1$ ) and two have redshifts that place the HI line within the lowest ASKAP band ( $0.4 < z < 1.0$ ). As for our BETA sample, we reduced the assumed redshift path for the two ‘in-band’ sources by  $\Delta z = 0.01$  to account for proximity effects. The total redshift interval probed for intervening DLA systems by the sources in Table 2 is  $\Delta z = 7.37$ . Two sources observed with BETA were re-observed with ASKAP-12, and these are also listed in Table 2.

### 2.3 Structure of the target radio sources

Our target sources were selected to be compact, and in most cases we expect their radio emission to be dominated by a single component with angular size smaller than 1 arcsec. We can assess this in several ways:

- **ATCA calibrators:** 50 of the 53 sources in Tables 1 and 2 are ATCA calibrator sources<sup>2</sup> listed in the online calibrator database.<sup>3</sup> For these sources, we can use the ‘de-

<sup>2</sup> The three objects not listed as ATCA calibrators are PKS 0743-67, PKS 1229-02 and PKS 2123-463

<sup>3</sup> [http://www.narrabri.atnf.csiro.au/calibrators/calibrator\\_database.html](http://www.narrabri.atnf.csiro.au/calibrators/calibrator_database.html)

**Table 1.** Targets observed with BETA

Name	RA	Dec	— Radio flux density (Jy) —				$z_{\text{em}}$	$z_{\text{ref}}$	$\Delta z$ probed <sup>a</sup>	Notes
			MRC	SUMSS	NVSS	AT20G				
(1)	(2)	(3)	(4)	(5)	(6)	(7)	(8)	(9)	(10)	(11)
PKS 0047-579	00:49:59.473	-57:38:27.34	2.52	2.05	...	1.87	1.797	Pe76	0.60	Background
PKS 0208-512	02:10:46.200	-51:01:01.89	5.48	3.37	...	3.29	1.003	Pe76	0.60	Background
PKS 0302-623	03:03:50.631	-62:11:25.55	0.86	2.46	...	1.31	1.351	He08	0.60	Background
PKS 0438-43	04:40:17.180	-43:33:08.60	8.12	5.86	...	1.95	2.863	Mo78	0.60	Background
PKS 0451-28	04:53:14.647	-28:07:37.33	2.14	...	2.54	1.79	2.559	Wi83	0.60	Background
PKS 0454-46	04:55:50.772	-46:15:58.68	4.25	2.87	...	4.16	0.853	Wi00	0.43	In-band
PKS 0506-61	05:06:43.989	-61:09:40.99	5.03	3.12	...	1.66	1.093	Wr77	0.60	Background
PKS 0537-441	05:38:50.362	-44:05:08.94	2.56	3.52	...	5.29	0.894	Pe76	0.47	In-band
PKS 0637-75	06:35:46.508	-75:16:16.82	7.89	5.38	...	3.14	0.653	Hu78	0.23	In-band
PKS 0743-67	07:43:31.612	-67:26:25.55	8.61	5.68	...	1.22	1.512	dS94	0.60	Background
PKS 0903-57	09:04:53.36	-57:35:04.7	4.90	3.31	...	1.43	...	..	( $\leq 0.6$ )	Uncertain <sup>b</sup>
PKS 0920-39	09:22:46.418	-39:59:35.07	4.38	3.16	2.62	1.31	0.591	Wh88	0.17	In-band
MRC 1039-474	10:41:44.650	-47:40:00.06	1.44	2.37	...	1.26	2.558	Ti13	0.60	Background <sup>b</sup>
PKS 1104-445	11:07:08.694	-44:49:07.62	1.49	2.52	...	1.67	1.598	Pe79	0.60	Background
PKS 1421-490	14:24:32.237	-49:13:49.74	13.10	9.68	...	2.64	0.662	Ma11	0.24	In-band
PKS 1424-41	14:27:56.298	-42:06:19.44	6.39	3.86	...	2.74	1.522	Wh88	0.60	Background
PKS 1504-167	15:07:04.787	-16:52:30.27	2.20	...	2.71	1.05	0.876	Hu78	0.45	In-band
MRC 1613-586	16:17:17.889	-58:48:07.86	3.12	3.10	...	2.71	1.422	Sh12	0.60	Background
PKS 1610-77	16:17:49.276	-77:17:18.47	5.35	4.15	...	1.86	1.710	Hu80	0.60	Background
PKS 1622-253	16:25:46.892	-25:27:38.33	2.36	...	2.52	2.06	0.786	dS94	0.35	In-band
PKS 1622-29	16:26:06.021	-29:51:26.97	2.74	...	2.29	1.79	0.814	NTT	0.39	In-band <sup>b</sup>
PKS 1740-517	17:44:25.451	-51:44:43.79	5.38	8.15	...	1.24	0.441	All15	0.02	In-band <sup>b</sup>
MRC 1759-396	18:02:42.680	-39:40:07.90	2.56	1.38	2.27	1.41	1.319	Sh12	0.60	Background <sup>b</sup>
PKS 1830-211	18:33:39.886	-21:03:40.57	11.47	...	10.90	5.50	2.507	Li99	0.60	Background
MRC 1908-201	19:11:09.653	-20:06:55.11	1.94	...	2.71	2.67	1.119	Ha03	0.60	Background
MRC 1920-211	19:23:32.190	-21:04:33.33	1.35	...	3.17	2.55	0.874	Ha03	0.45	In-band
PKS 2052-47	20:56:16.360	-47:14:47.63	4.15	2.14	...	1.17	1.492	Mu84	0.60	Background
PKS 2155-152	21:58:06.282	-15:01:09.33	2.51	...	3.02	1.90	0.672	Wh88	0.25	In-band
PKS 2203-18	22:06:10.417	-18:35:38.75	9.73	...	6.40	2.03	0.619	Mo82	0.19	In-band
PKS 2326-477	23:29:17.704	-47:30:19.12	3.21	3.05	...	1.42	1.304	6dF	0.60	Background
PKS 2333-528	23:36:12.145	-52:36:21.95	1.81	2.16	...	1.07	...	..	( $\leq 0.6$ )	Uncertain
PKS 2345-16	23:48:02.609	-16:31:12.02	2.09	...	2.64	2.45	0.576	Ta93	0.15	In-band

Total path length for the 30 sources of known redshift:  $\Delta z(\text{BETA}) = 14.00$

Redshift references ( $z_{\text{ref}}$ ): 6dF=6dF Galaxy Survey (Jones et al. 2009); All15=Allison et al. (2015); dS94=di Serego-Alighieri et al. (1994); Ha03=Halpern et al. (2003); He08=Healey et al. (2008); Hu78=Hunstead et al. (1978); Hu80=Hunstead & Murdoch (1980); Li99=Lidman et al. (1999); Ma11=Marshall et al. (2011); Mo78=Morton et al. (1978); Mo82=Morton & Tritton (1982); Mu84=Murdoch et al. (1984); NTT=ESO NTT spectrum, this paper (see Appendix); Pe76=Peterson et al. (1976); Pe79=Peterson et al. (1979); Sh12=Shaw et al. (2012); Ta93=Tadhunter et al. (1993); Ti13=Titov et al. (2013); Wh88=White et al. (1988); Wi83=Wilkes et al. (1983); Wi00=Wisotzki et al. (2000); Wr77=Wright et al. (1977).

Position measurements are from the ICRF VLBI catalogue (Ma et al. 1998) except for the following: PKS 0903-57 position from Murphy et al. (2010); MRC 1039-474 from Titov et al. (2013) PKS 1421-490 and MRC 1613-586 from Petrov et al. (2011); MRC 1759-396 from Fomalont et al. (2003); PKS 1830-211 from Fomalont et al. (2000), PKS 2203-18 from Beasley et al. (2002).

<sup>a</sup> For 'in-band' radio sources with redshift  $z \leq 1.0$ , we exclude a region within  $3000 \text{ km s}^{-1}$  of the emission redshift (column 8) since this region may be occupied by associated systems.

<sup>b</sup> See notes on individual objects in Appendix A.

**Table 2.** Targets observed with ASKAP-12

Name (1)	RA (2)	Dec (J2000) (3)	— Radio flux density (Jy) —				$z_{\text{em}}$ (8)	$z_{\text{ref}}$ (9)	$\Delta z$ probed <sup>a</sup> (10)	Notes (11)
			MRC (4)	SUMSS (5)	NVSS (6)	AT20G (7)				
(a) New targets										
PKS 0122-00	01:25:28.844	−00:05:55.93	1.20	...	1.54	1.16	1.075	6dF	0.40	Background
PKS 0237-23	02:40:08.175	−23:09:15.73	3.67	...	6.26	0.90	2.223	Ar67	0.40	Background
PKS 0405-12	04:07:48.431	−12:11:36.66	8.17	...	2.94	1.25	0.573	Ma96	0.18	In-band
PKS 0454-234	04:57:03.179	−23:24:52.02	...	...	1.73	3.84	1.003	St89	0.40	Background
PKS 0458-02	05:01:12.810	−01:59:14.26	2.30	...	2.26	1.10	2.286	St74	0.40	Background
PKS 0805-07	08:08:15.536	−07:51:09.89	2.49	...	1.60	0.77	1.837	Wh88	0.40	Background
PKS 0834-20	08:36:39.215	−20:16:59.50	3.53	...	1.97	2.67	2.752	Fr83	0.40	Background
PKS 0859-14	09:02:16.831	−14:15:30.88	3.93	...	2.90	1.04	1.332	6dF	0.40	Background <sup>b</sup>
PKS 1127-14	11:30:07.053	−14:49:27.39	5.07	...	5.62	1.87	1.184	Wi83	0.40	Background
PKS 1136-13	11:39:10.703	−13:50:43.64	10.50	...	4.22	0.54	0.556	6dF	0.16	In-band
PKS 1144-379	11:47:01.371	−38:12:11.02	0.94	0.81	1.80	1.38	1.048	St89	0.40	Background
PKS 1229-02	12:32:00.016	−02:24:04.80	3.87	...	1.65	0.90	1.045	He10	0.27 <sup>c</sup>	Background
PKS 1245-19	12:48:23.898	−19:59:18.59	8.61	...	5.14	0.69	1.275	O'D91	0.40	Background <sup>b</sup>
PKS 1508-05	15:10:53.592	−05:43:07.42	7.71	...	3.57	1.27	1.185	Wi86	0.36 <sup>c</sup>	Background
PKS 1935-692	19:40:25.528	−69:07:56.97	1.70	1.75	...	0.52	3.154	Os94	0.40	Background
PKS 2106-413	21:09:33.189	−41:10:20.61	2.66	1.82	...	1.63	1.058	Wh88	0.40	Background
PKS 2123-463	21:26:30.704	−46:05:47.89	1.95	1.52	...	0.55	...	..	( $\leq 0.4$ )	Uncertain <sup>b</sup>
PKS 2131-021	21:34:10.310	−01:53:17.24	1.91	...	1.69	2.11	1.285	Dr97	0.40	Background
PKS 2204-54	22:07:43.733	−53:46:33.82	2.55	1.80	...	1.12	1.215	Wi83	0.40	Background
PKS 2223-05	22:25:47.259	−04:57:01.39	11.89	...	7.41	8.32	1.404	Wr83	0.40	Background <sup>b</sup>
PKS 2244-37	22:47:03.917	−36:57:46.30	2.95	1.71	1.26	0.94	2.252	Wi83	0.40	Background
Total path length for the 20 sources of known redshift: $\Delta z(\text{ASKAP-12}) = 7.37$										
(b) Repeat observations of BETA targets										
PKS 1610-77	16:17:49.276	−77:17:18.47	5.35	4.15	...	1.86	1.710	Hu80	0.40	Background
PKS 1830-211	18:33:39.886	−21:03:40.57	11.47	...	10.90	5.50	2.507	Li99	0.40	Background
MRC 1908-201	19:11:09.653	−20:06:55.11	1.94	...	2.71	2.67	1.119	Ha03	0.40	Background

Redshift references ( $z_{\text{ref}}$ ): 6dF=6dF Galaxy Survey (Jones et al. 2009); Ar67=Arp et al. (1967); Dr97=Drinkwater et al. (1997) Fr83=Fricke et al. (1983); Ha03=Halpern et al. (2003); He10=Hewett & Wild (2010); Hu80=Hunstead & Murdoch (1980); Li99=Lidman et al. (1999); Ma96=Marziani et al. (1996); O'D91=O'Dea et al. (1991); Os94=Osmer et al. (1994); St74=Strittmatter et al. (1974); St89=Stickel et al. (1989); Wh88=White et al. (1988); Wi83=Wilkes et al. (1983); Wi86=Wilkes (1986); Wr83=Wright et al. (1983).

Position measurements are from the ICRF VLBI catalogue (Ma et al. 1998) except for the following: PKS 0122-00 and PKS 1136-13 from Beasley et al. (2002); PKS 1229-02, PKS 1245-19, PKS 1508-05, PKS 2123-463 and PKS 2244-37 from Fey et al. (2015).

<sup>a</sup> For ‘in-band’ radio sources with redshift  $z \leq 0.77$ , we exclude a region within  $3000 \text{ km s}^{-1}$  of the emission redshift (column 8) since this region may be occupied by associated systems.

<sup>b</sup> See notes on individual objects in Appendix A.

<sup>c</sup> For PKS 1229-02 and PKS 1508-05, the redshift path probed was reduced slightly due to correlator errors over part of the observed frequency range.

fect’ and ‘closure phase’ parameters listed in the calibrator database to identify any sources that have resolved emission on arcsec scales at frequencies above 1.4 GHz.

- **AT20G 6-km visibilities:** 48 of the 53 sources have visibility measurements at 20 GHz on the longest (6 km) ATCA baselines (Chhetri et al. 2013), which allow us to assess the compactness of sources on scales of  $\sim 150$  mas.

- **VLBI images:** 36 of the sources in Tables 1 and 2 have VLBI images from Ojha et al. (2005, 2010) or Pushkarev

et al. (2017) that map out the structure of compact components on scales as small as 1-10 mas.

While these data are useful, they provide at best an imperfect picture of the structure of these sources in the frequency range observed by ASKAP. As noted by Kanekar et al. (2014), we would ideally like to have lower-frequency VLBI images that allow us to estimate what fraction of the 700-1000 MHz radio emission seen by ASKAP (which had  $\sim 1$  arcmin resolution at the time of our commissioning ob-

servations) is located in compact components less than 10–20 mas in angular size.

Table 3 lists galaxies in our sample that are known to have some resolved continuum emission on arcsec scales (though each of these objects also has a strong compact core). These objects were identified either because the ATCA calibrator database showed evidence for structure on arcsecond scales, or because the Chhetri et al. (2013) 6-km visibility had a value  $< 0.9$ , indicating the presence of resolved emission on scales larger than about 0.15 arcsec. We then carried out a literature search for arcsec-scale radio images of these objects, and the results are summarized in column (5) of Table 3. PKS 1830-211, also listed in this table, is a special case since the resolved emission is the result of gravitational lensing by a foreground galaxy, rather than being intrinsic to the source.

Most of the sources with published VLBI images at 5–15 GHz (Ojha et al. 2005, 2010; Pushkarev et al. 2017; Petrov et al. 2019) appear to have a significant fraction (typically 20–60%) of their flux density in components smaller than  $\sim 10$  mas. This corresponds to an angular scale of roughly 50 pc at  $z \sim 0.4$ , 70 pc at  $z \sim 0.7$  and 80 pc at  $z \sim 1.0$ , which is slightly smaller than the expected size of individual HI clouds in galaxy disks (estimated as  $\sim 100$  pc; Braun 2012). Even without a more detailed knowledge of the source structure, therefore, it appears that most of our target sources remain quite compact on scales as small as 10–20 mas, making them effective probes for intervening HI absorption-line systems (because there is less need to account for a non-unity covering factor  $f$ ).

This conclusion is supported by the work of Horiuchi et al. (2004), who observed a large sample of powerful flat-spectrum radio AGN at 5 GHz with both the VLBA and VSOP. They found that a typical AGN in their sample had about 50% of its radio emission in a component smaller than 10 mas in size, with around 40% of this milliarcsec-scale emission (20% of the total emission) coming from a radio core with an average size of 0.2 mas.

### 3 OBSERVATIONS

The observational techniques and data reduction used were similar to those described by Allison et al. (2015) and Allison et al. (2017), and we refer the reader to those papers for further details.

#### 3.1 Observations with BETA

We observed the 32 objects listed in Table 1 with BETA over the period from July 2014 to February 2016. The total integration time was typically 3–5 hours for each object, with between 4 and 6 BETA dishes in the array. The BETA telescope was used as an engineering testbed throughout its operation, so there were sometimes technical problems that made part or all of an observation unusable. When this occurred, the observation was repeated until good-quality data were obtained.

In principle up to nine beams could be formed for wide-field imaging using the Mark I phased array feeds (PAFs) on BETA, positioned anywhere within the  $30 \text{ deg}^2$  field of

view of the PAF. However, for our targeted observations presented here, we used a single PAF beam centred at the position of the target source. To obtain initial solutions for the complex antenna gains and to calibrate the flux density scale (based on the model of Reynolds 1994), we accompanied each observation with a short integration on PKS B1934–638 between 5 and 15 min. The expected uncertainty in the flux density scale is 2–3% (Heywood et al. 2016).

Our observations with BETA were carried out exclusively using the lower frequency band, between 711.5 and 1015.5 MHz, equivalent to HI redshifts between  $z_{\text{HI}} = 0.4$  and 1.0. The fine channelization generated 16,416 channels across the 304 MHz bandwidth, with an effective spectral resolution between approximately 5.5 and  $7.8 \text{ km s}^{-1}$ . The full width at half power of the PAF beams is approximately 1.7 degrees at the band centre, and the spatial resolution of BETA is approximately 1 arcminute (using uniform weighting) so that we do not expect any of our objects to be spatially resolved.

#### 3.2 Observations with ASKAP-12

We observed the 23 objects listed in Table 2 with ASKAP-12 during January–February 2017. The total integration time was typically 2 hours for each object. ASKAP-12 usually had between 12 and 14 antennas operational for each observation, each fitted with Mark II PAFs with improved sensitivity at 1400 MHz (see Chippendale et al. 2015).

Up to 36 PAF beams could be electronically formed to fully sample the  $30 \text{ deg}^2$  field of view. However, for our observations we only considered a single beam centred on the object source. Since calibration of the complex antenna gains and flux scale in each PAF beam would require a separate observation of PKS 1934–638, only forming a single beam greatly improves observing efficiency for this work. Secondly, during commissioning observations the ASKAP-12 backend capacity was limited so that forming a single PAF beam allowed us to achieve a larger spectral bandwidth.

We observed simultaneously at all frequencies between 799.5 and 1039.5 MHz, spanning HI redshifts between  $z_{\text{HI}} = 0.37$  and 0.77. The fine channelisation produced 12960 channels across the 240 MHz, with an effective spectral resolution between 5.3 and  $6.9 \text{ km s}^{-1}$ . The PAF beam full width at half power at the band centre is approximately 1.6 degrees and the spatial resolution is approximately 30 arcsec, again meaning that none of our targets are expected to be spatially resolved by these observations.

#### 3.3 Data reduction

The ingested data from the ASKAP correlator were recorded in measurement set format and so initial flagging (autocorrelations and amplitude thresholding) and splitting of the data were performed using the CASA package (McMullin et al. 2007). Subsequent automated flagging, calibration, imaging and continuum subtraction of the data were carried out using the MIRIAD package (Sault et al. 1995).

The full-spectral-resolution visibilities were split into sub-band chunks, so as to enable efficient parallelization of the data processing and to remove spectral discontinuities caused by the PAF beams. The PAF beams were formed

**Table 3.** Sources known to have resolved continuum emission on arcsec scales. Column 4 lists the 20 GHz visibilities on the longest (6-km) ATCA baseline, from [Chhetri et al. \(2013\)](#). Sources with  $6k\_vis \geq 0.9$  are expected to have almost all their high-frequency radio emission originating from a region less than about 120 mas in angular size.

Name (1)	$z_{ref}$ (2)	Cal? (3)	$6k\_vis$ (4)	Notes (5)	Ref. (6)
PKS 0405-12	0.573	C	0.94	Triple at 1.4 GHz, strong core, LAS~ 40 arcsec	Sa04
PKS 0903-57	..	C	0.69	Compact double at 5 GHz, LAS ~ 3 arcsec	Ma05
PKS 1136-13	0.556	C	0.45	Triple at 1.4 GHz, strong core, LAS~ 20 arcsec	Sa04
PKS 1229-02	1.045	..	0.89	Triple at 1.6 GHz, LAS ~ 20 arcsec	Kr92
PKS 1421-490	0.662	C	0.76	Strong core at 5 GHz with ~ 1 arcsec jet	Ma05
PKS 2123-463	..	...	0.91	Two components at 5 GHz, LAS~ 4 arcsec	Mc12
PKS 1830-211	2.507	C	0.19	Lensed double/ring at 1.7 GHz, LAS~ 1 arcsec	Ja91

References: Hi83=[Hintzen et al. \(1983\)](#); Ja91=[Jauncey et al. \(1991\)](#); Kr92=[Kronberg et al. \(1992\)](#); Ma05=[Marshall et al. \(2005\)](#); Mc12=[McConnell et al. \(2012\)](#); Sa89=[Saikia et al. \(1989\)](#); Sa04=[Sambruna et al. \(2004\)](#)

electronically in fixed frequency intervals; every 4 or 5 MHz for BETA and 1 MHz for ASKAP-12. These generated discontinuous jumps in the complex gain response of the telescope as a function of frequency and therefore needed to be corrected during bandpass calibration and refined further in continuum subtraction. In the case of BETA, these intervals equate to velocities greater than  $1000 \text{ km s}^{-1}$  and are therefore much larger than the typical linewidths expected for absorption. We corrected for this simply by splitting the data into sub-band chunks and performing bandpass calibration and continuum subtraction individually on these data.

However, in the case of the 1 MHz intervals used in ASKAP-12 this approach could lead to removal of absorption lines wider than  $300 \text{ km s}^{-1}$  during continuum subtraction. We therefore split the ASKAP-12 data into sub-band chunks of 4 MHz (i.e. four beamforming intervals). To correct for the discontinuities in ASKAP-12 data that occur every 1 MHz, we solved for the bandpass per channel using PKS 1934-638 and then recovered S/N by using GPEDIT to smooth the solutions using a 10-channel Hanning window with a break every 1 MHz. Outliers in the bandpass solutions, which are generated either by hardware glitches or radio frequency interference, were identified using the interquartile range and replaced through interpolation before smoothing.

Separately, a single full-bandwidth data set, averaged to 1 MHz resolution, was used to obtain high signal-to-noise continuum images for self-calibration. Initial solutions to the antenna gains as a function of time were obtained using a sky model based on the catalogues of SUMSS ([Mauch et al. 2003](#)), MGPS2 ([Murphy et al. 2007](#)) and NVSS ([Condon et al. 1998](#)). Further iterative refinement of the solutions to smaller time intervals were then carried out using self-calibration based on the imaged continuum data. These gain solutions were then applied to the full-spectral-resolution data in each sub-band chunk.

Continuum subtraction was carried out separately on each sub-band chunk; first using the CLEAN algorithm to generate a continuum model, which was then subtracted from the visibilities using UVMODEL, followed by UVLIN to fit and subtract a second order polynomial from the residuals. Data cubes were formed by imaging the continuum-

subtracted visibilities in each sub-band chunk and a single spectrum was constructed at the position of peak emission from the continuum source. The continuum flux density was also measured at the same position in each sub-band chunk, so that the fractional absorption could be accurately calculated as a function of frequency. In cases where an object was observed on multiple occasions we formed a single spectrum by carrying out an inverse-variance-weighted average.

### 3.4 Data tables

Tables 4 and 5 list some key parameters of the objects observed with BETA and ASKAP-12 respectively, arranged as follows:

- (1) Source name from Table 1 or 2
- (2) Total observing time (in hours)
- (3) Mean continuum flux density of the source (in mJy) averaged across the full continuum frequency band observed
- (4) Standard deviation of the mean flux density - for these strong sources, this is a mainly a measure of how much the continuum flux density varies across the 240–300 MHz band
- (5) Typical (median) rms noise (in mJy) in a single spectral channel
- (6) Typical  $1\sigma$  sensitivity in optical depth for a single spectral channel.

### 3.5 Quality of the ASKAP radio spectra

Figure 1 shows a full ASKAP-12 spectrum of one of our target sources, PKS 0237-23. The quality of the spectrum is typical of those obtained during commissioning time, and the band is completely free of terrestrial and satellite-generated RFI.

The rms noise level in this spectrum is roughly constant with frequency across the full 288 MHz ASKAP band, giving a similar detection sensitivity at all redshifts sampled, and this is also true of the radio spectra of our other BETA and ASKAP-12 target sources. However, in the case of ASKAP-12 we found an error in the firmware weights that are used to correct the 1-MHz channelisation. This generates features at

**Table 4.** Measurements from BETA observations of the target sources in Table 1. See §3.4 of the text for a description of each column. For objects with more than one observation, the values listed are for the spectrum with the best optical-depth sensitivity  $\sigma_\tau$ .

Name	t	$S_{\text{cont}}$	$\Delta S$	rms/ch	$\sigma_\tau$
(1)	(h)	mJy	mJy	mJy	(6)
PKS 0047-579	5	2198	81	21.7	0.0099
PKS 0208-512	3	2748	163	30.3	0.0110
PKS 0302-623	5	4426	429	43.0	0.0097
PKS 0438-43	3	5455	354	37.2	0.0068
PKS 0451-28	5	2430	94	23.4	0.0096
PKS 0454-46	5	3680	130	22.9	0.0062
PKS 0506-61	3.5	3154	263	31.0	0.0098
PKS 0537-441	5	4318	183	22.8	0.0053
PKS 0637-75	4	6250	663	26.4	0.0042
PKS 0743-67	4	5276	407	24.2	0.0046
PKS 0903-57	3	3156	194	28.4	0.0090
PKS 0920-39	5	3233	152	25.5	0.0079
MRC 1039-474	5	1867	77	24.4	0.0130
PKS 1104-445	4	2417	502	25.0	0.0103
PKS 1421-490	2	9360	512	36.3	0.0039
PKS 1424-41	3.5	4714	153	27.9	0.0059
PKS 1504-167	5	1634	73	23.6	0.0144
MRC 1613-586	5	4586	104	24.4	0.0053
PKS 1610-77	5	3933	206	16.5	0.0042
PKS 1622-253	5	2222	102	29.5	0.0133
PKS 1622-29	5	2755	115	23.7	0.0086
PKS 1740-517					
MRC 1759-396	4	1489	29	29.0	0.0195
PKS 1830-211	3.5	12620	521	37.6	0.0030
MRC 1908-201	5	1768	57	23.7	0.0134
MRC 1920-211	5	2331	175	24.8	0.0106
PKS 2052-47	5	2523	140	22.1	0.0088
PKS 2155-152	5	4096	88	24.9	0.0061
PKS 2203-18	3	7395	416	58.0	0.0078
PKS 2326-477	4	4169	151	35.3	0.0085
PKS 2333-528	5	2233	58	26.8	0.0120
PKS 2345-16	5	2684	39	27.4	0.0102

the level of 1 per cent in gain amplitude every 1 MHz, which we account for when assessing detection reliability.

### 3.6 Detection limits and sensitivity

As can be seen from Tables 3 and 4, the rms noise in our spectra was typically 20–30 mJy per spectral channel for BETA observations and around 12 mJy per channel for observations with ASKAP-12. This corresponds to a  $5\sigma$  detection limit in optical depth of around 0.05 for BETA and 0.02 for ASKAP-12.

Figure 2 plots the detection limits in HI column density for each of the spectra in Tables 1 and 2, assuming a covering

**Table 5.** Measurements from ASKAP-12 observations of the target sources in Table 2. See §3.4 of the text for a description of each column.

Name	t	$S_{\text{cont}}$	$\Delta S$	rms/ch	$\sigma_\tau$
(1)	(2)	(3)	(4)	(5)	(6)
PKS 0122-00	2	1633	75	12.6	0.0078
PKS 0237-23	2	6824	258	12.6	0.0018
PKS 0405-12	2	2638	50	12.5	0.0044
PKS 0454-234	2	2020	10	12.3	0.0061
PKS 0458-02	2	1376	13	15.1	0.0110
PKS 0805-07	2	1895	27	13.6	0.0072
PKS 0834-20	2	2492	21	12.8	0.0051
PKS 0859-14	2	3992	67	12.7	0.0032
PKS 1127-14	2	6268	81	12.8	0.0021
PKS 1136-13	2	6016	265	12.2	0.0020
PKS 1144-379	2	1415	76	12.4	0.0088
PKS 1229-02	2	1927	121	13.1	0.0069
PKS 1245-19	2	6644	338	12.1	0.0013
PKS 1508-05	2	5248	100	12.8	0.0024
PKS 1935-692	2	1641	39	16.2	0.0064
PKS 2106-413	2	1790	13	12.4	0.0069
PKS 2123-463	2	1521	46	11.3	0.0075
PKS 2131-021	2	1957	14	11.1	0.0057
PKS 2204-54	2	2356	20	11.9	0.0050
PKS 2223-05	2	8356	359	21.9	0.0012
PKS 2244-37	2	1581	87	10.9	0.0069
Repeat observations					
PKS 1610-77	2	3584	134	12.7	0.0035
MRC 1908-201	2	1968	76	13.0	0.0066

factor  $f = 1$  and HI spin temperatures of 100 K (blue points) and 600 K (red points). For  $T_s = 100$  K, we should be able to detect a minimal DLA absorber with  $N_{\text{HI}} \sim 2 \times 10^{20} \text{ cm}^{-2}$  for all our targets across the full range of redshifts probed. The red points in Figure 2 are included to show that DLAs with spin temperatures above about 600 K are unlikely to be detectable in the current pilot survey.

Figure 3 gives a more detailed look at the redshift and spin-temperature sensitivity of the sample as a whole. In these plots, the vertical axis shows the fraction of our sightlines on which we could detect (a) a sufficiently-strong intervening HI absorption line at redshift  $z$ , and (b) a minimal DLA system (with  $N_{\text{HI}} = 2 \times 10^{20} \text{ cm}^{-2}$  and covering factor  $f = 1$ ). This ‘fraction of sightlines’ roughly corresponds to the total redshift path-length  $\Delta z$  over which each kind of line could be detected in our survey. While this path-length is roughly constant with redshift (dropping off at  $z > 0.8$  because of the frequency limit of the ASKAP-12 spectra), the right-hand plot shows that (as expected for a 21 cm survey) we are much more sensitive to absorption lines from gas with a low HI spin temperature than to lines that originate in warmer gas. Figure 3 shows that that our 50% completeness corresponds to  $T_s \sim 300$  K. We note that this is similar

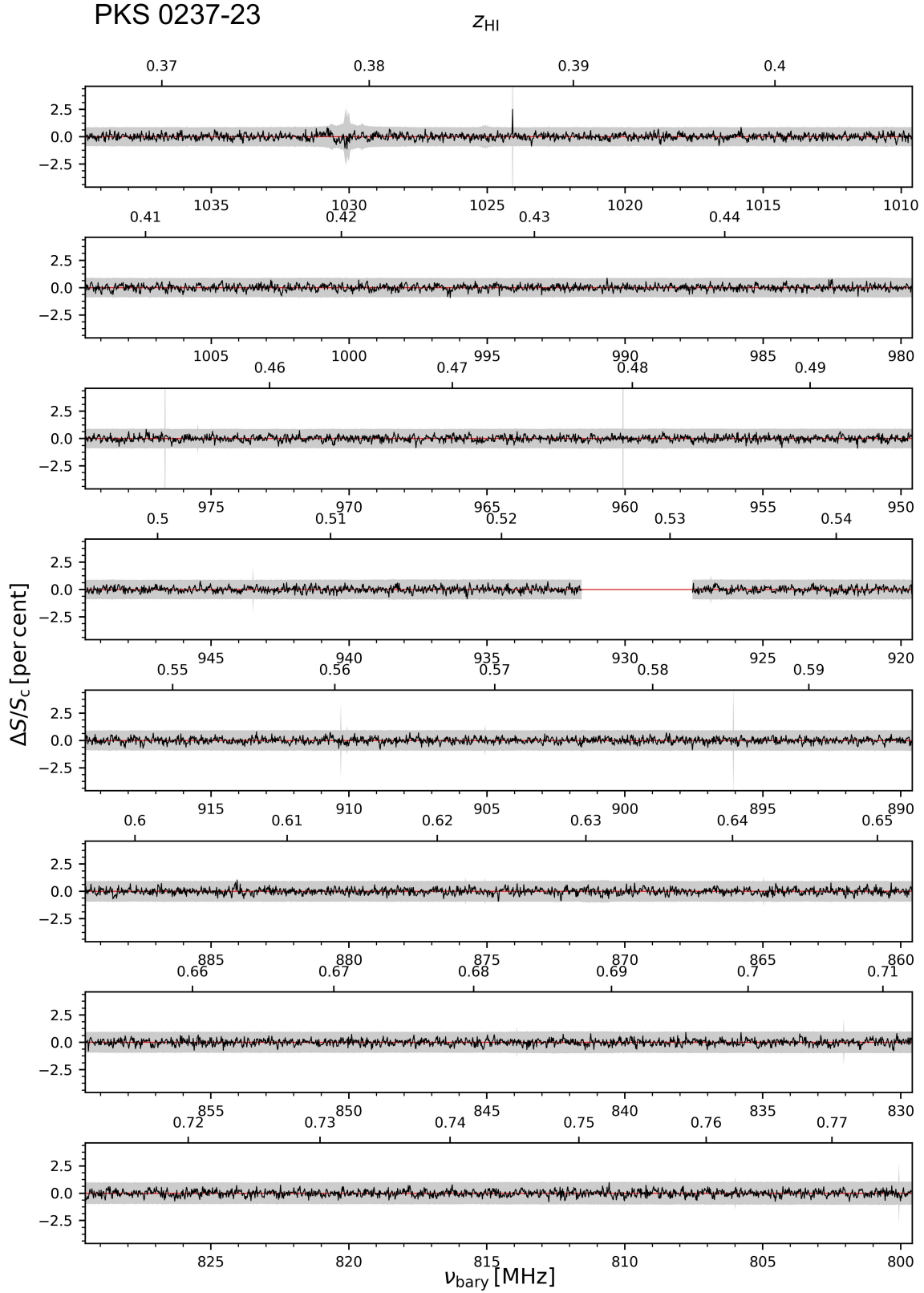


**Figure 1.** The full ASKAP-12 spectrum of PKS0237-23 (AT20G J024008-230916), a radio-loud quasar at  $z = 2.223$ . The median rms noise in this spectrum is 12.6 mJy per 18 kHz channel. Some noise spikes are visible, and one small region (near 930 MHz) is missing data because of a correlator-block failure. The light-grey band is set at  $\pm 5$  times the rms noise.

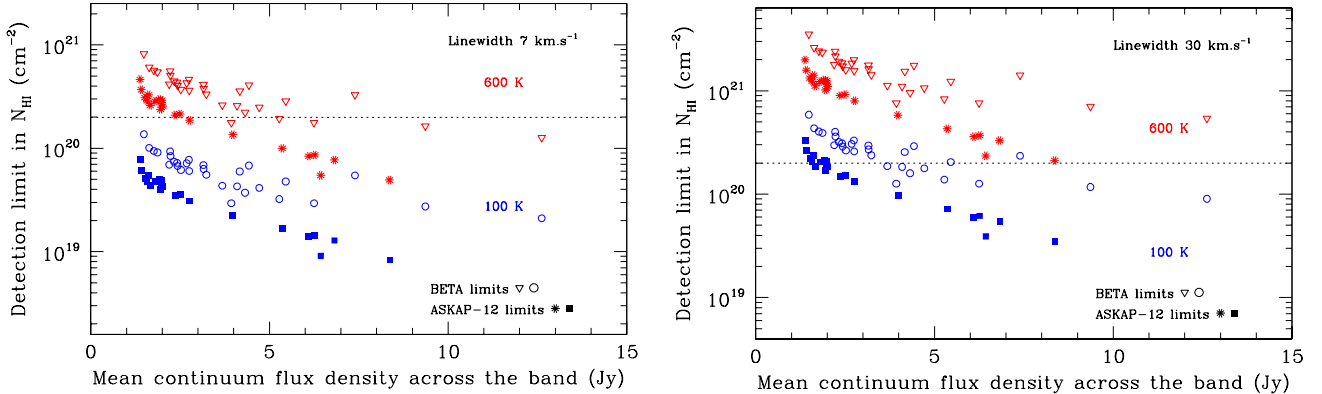


**Figure 2.** Detection limits in HI column density for the observations in Tables 1 and 2, assuming a covering factor  $f = 1$ , and a spin temperature of 100 K (blue squares and open circles) or 600 K (red stars and open triangles). The left-hand plot assumes a  $5\sigma$  detection limit for a narrow line of width  $7 \text{ km s}^{-1}$ , while the right-hand plot shows a  $5.5\sigma$  detection limit for a broader line with a width of  $30 \text{ km s}^{-1}$  as discussed by Allison et al. (2020). The horizontal dotted line in each plot shows the DLA column density limit of  $2 \times 10^{20} \text{ cm}^{-2}$ .

to the harmonic mean spin temperature of the Milky Way ISM Murray et al. (2018).

## 4 RESULTS

### 4.1 Detection of redshifted 21 cm absorption lines

The total path-length over which we could detect 21 cm absorption lines was  $\Delta z = 21.37$  for the 50 background radio sources with known optical redshifts. We made no prior assumptions about the redshift of any line, so this is a genuinely ‘blind’ line search in the spectral domain.

We used the Bayesian detection method developed by Allison et al. 2012 to search for absorption lines in the spectrum. This method uses the Bayes factor to assign significance to a particular feature in the spectrum, equal to ratio of the Bayesian evidences for a Gaussian line and noise model, versus a null model comprising just the noise. We consider all features with values greater than  $\ln \text{Bayesfactor} > 1$ . Given the aforementioned error from applying incorrect coarse-channelisation weights, and failures of individual correlator cards, further visual inspection of detected features was required. Upon inspection, we obtained four reliable detections of intervening absorption lines and one associated absorption line along the line of sight to the 53 radio sources listed in Tables 1 and 2.

The associated absorption-line system, at  $z = 0.44$  in PKS 1740-517, has been studied in detail by Allison et al. (2015) and Allison et al. (2019) and is not discussed further in this paper.

The properties of the four intervening absorption lines are summarised in Table 6 and discussed below. Two of these lines (towards PKS 0834-20 and PKS 1610-77) are new detections, while the other two are re-detections of previously-known absorption-line systems.

### 4.2 Intervening HI absorption towards PKS 0834-20

We made a new detection of 21 cm HI absorption at  $z = 0.591$  along the line of sight to the background ( $z = 2.75$ ) radio

source PKS 0834-20. Figure 4 shows the ASKAP spectrum at the position of the absorption line. The peak optical depth of this line ( $\tau = 0.14$ ) is the highest out of our four ASKAP detections.

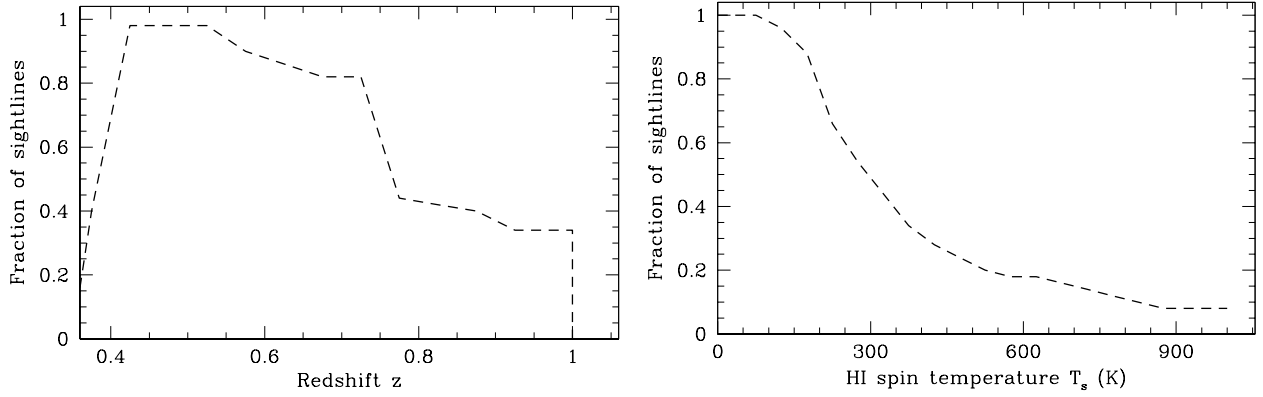
The background radio source, PKS 0834-20 is a radio-loud blazar, and low-frequency observations show a broad peak in the radio spectrum near 500 MHz (Callingham et al. 2017). The 15 GHz VLBA continuum image published by the MOJAVE team (Pushkarev et al. 2017) shows a core-jet structure with a total extent of 6.4 mas, corresponding to 42 pc at the redshift of the 21 cm absorption line.

### 4.3 Intervening absorption towards PKS 1229-02

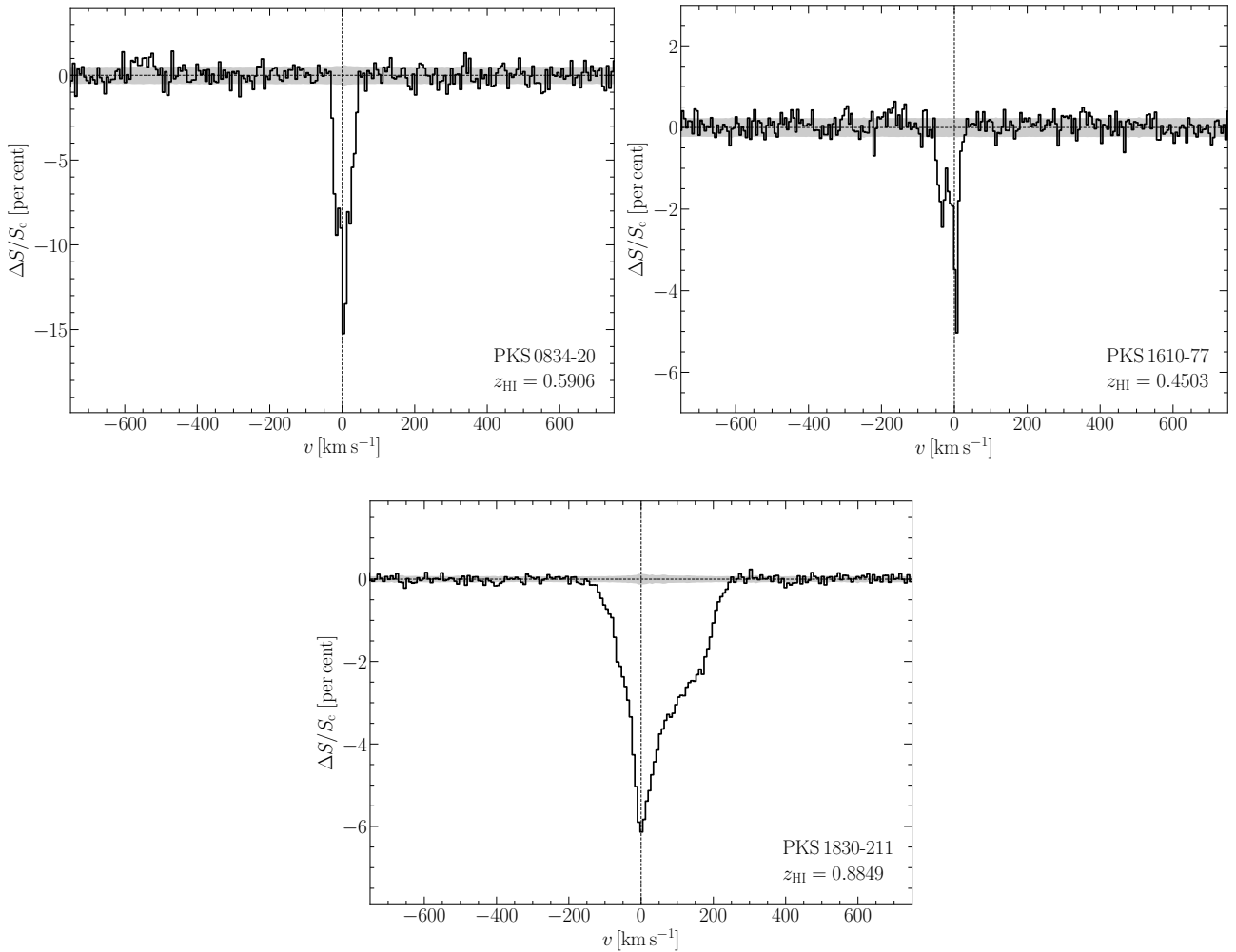
A 21 cm HI absorption line at  $z = 0.395$  was first detected along a sightline to PKS 1229-02 by Brown & Spencer (1979) with the NRAO 140-ft (43 m) single-dish radio telescope, and this observation was motivated by the presence of strong Mg II absorption in the optical spectrum (Kinman & Burbidge 1967). Wolfe (1980) detected the same HI absorption line with the Arecibo telescope, again using Mg II pre-selection.

Figure 5 shows the ASKAP detection of intervening 21 cm absorption at  $z = 0.395$  along the line of sight to the radio-loud QSO PKS 1229-02. The original ASKAP-12 detection had relatively low S/N, and the measured optical depth of the HI line was significantly lower than the values observed by Brown & Spencer (1979) and Wolfe (1980). To test whether this was the result of variability in the line profile over time, we re-observed PKS 1229-02 in a test observation for 8 hours with the full 36-antenna ASKAP array in May 2019. The new ASKAP-36 spectrum is also shown in Figure 5. The total integration time for the ASKAP-36 spectrum was 8 hours, and the HI optical depth measured from this higher-quality ASKAP spectrum is similar to the Brown & Spencer (1979) and Wolfe (1980) values.

The PKS 1229-02 absorption system is well-studied at optical and UV wavelengths. The strong metal absorption lines in the optical spectrum at  $z = 0.395$  have been studied by Briggs et al. (1985) and Lanzetta & Bowen (1992), and imply a relatively high metallicity for the absorbing gas.



**Figure 3.** (left) Fractional redshift coverage for the radio sources in Tables 1 and 2. This is set mainly by the frequency range used for the BETA and ASKAP-12 observations, so we probe fewer sightlines at  $z > 0.77$ . (right) The fraction of sightlines for which we could detect (at the  $5\text{-}\sigma$  level) a minimal DLA system with  $N_{\text{HI}} = 2 \times 10^{20} \text{ cm}^{-2}$ , assuming a line width  $7 \text{ km s}^{-1}$  and covering factor  $f = 1$ . For spin temperatures above 250-300 K, detections of most DLA systems are only possible against the strongest continuum sources in our sample.



**Figure 4.** Intervening absorption lines detected by ASKAP towards the radio sources PKS 0834-20, PKS 1610-77 and PKS 1830-211. The grey shading in each plot shows  $\pm\tau_{\text{lim}}$ , where  $\tau_{\text{lim}}$  is the  $1\sigma$  limit in optical depth listed in Tables 4 and 5.

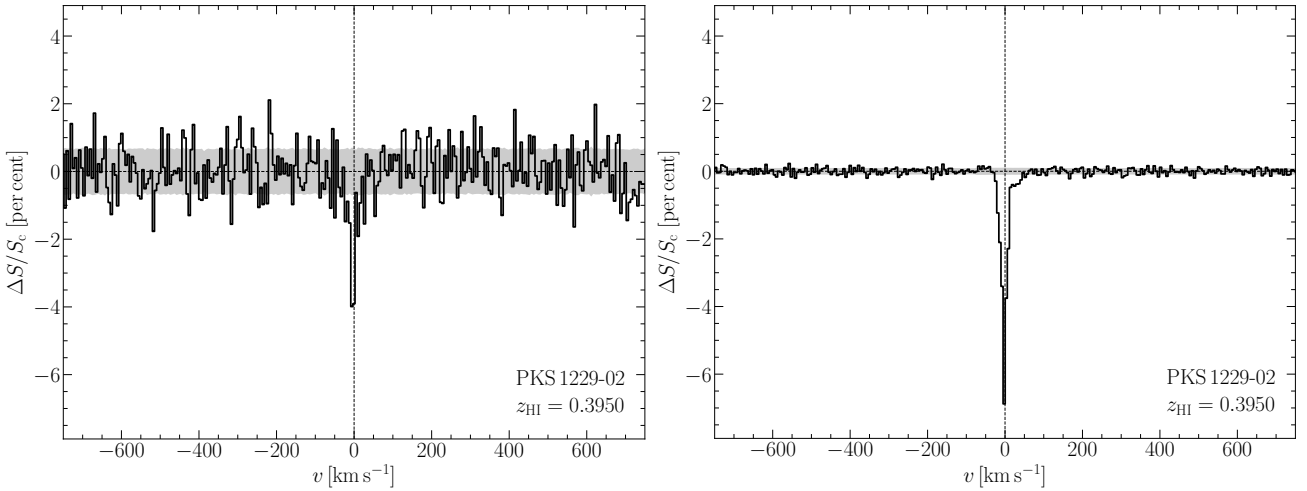


**Figure 5.** Intervening absorption at  $z = 0.3950$  along the line of sight to the background radio source PKS 1229-02 at  $z = 1.045$ . (left) The original ASKAP-12 spectrum, (right) A new ASKAP-36 spectrum of the same sightline. The grey shading shows  $\pm\tau_{\text{lim}}$ , where  $\tau_{\text{lim}}$  is the  $1\sigma$  limit in optical depth listed in Tables 4 and 5.

The PKS 1229-02 absorption system is the only one in our current sample for which an HI column density has also been measured from the Ly $\alpha$  line. Boissé et al. (1998) used the HST to observe the damped Lyman- $\alpha$  line in the UV at  $z = 0.395$ , from which they measured an HI column density of  $N_{\text{HI}} = 5.6 \times 10^{20} \text{ cm}^{-2}$ . In principle, this allows us to measure the HI spin temperature  $T_s$  if we assume that the Ly $\alpha$  and 21 cm absorption measurements are along the same sightline. Unlike most of the other sources in our sample, PKS 1229-02 contains extended radio structure on scales out to  $\sim 18$  arcsec (Hintzen et al. 1983; Kronberg et al. 1992) in addition to a compact central source. This complicates the analysis of the absorption-line spectrum, and we adopt the covering factor of  $f = 0.42$  derived by Kanekar et al. (2009).

From our ASKAP spectrum, we derive a value of  $T_s = 102 \pm 12$  K for the PKS 1229-02 absorption system. This is consistent with the previously-published estimates of  $T_s$  summarized in Table 7, which range from 95 to 170 K.

#### 4.4 Intervening absorption towards PKS 1610-77

With BETA, we made a new detection of intervening 21 cm absorption at  $z = 0.4503$  along the line of sight to the radio-loud QSO PKS 1610-77, as shown in Figure 4. The line has at least two velocity components, with a separation of  $\approx 30 \text{ km s}^{-1}$ .

The VLBI image published by Ojha et al. (2010) shows a curved jet extending about 5 mas from the core, along with some diffuse emission on larger scales. At the redshift of the HI absorption line, the angular extent of this jet corresponds to a linear size of  $\sim 30$  pc.

#### 4.5 Intervening absorption towards PKS 1830-211

PKS 1830-211 is a gravitationally-lensed radio source (Subrahmanyan et al. 1990; Jauncey et al. 1991) with an intervening galaxy at  $z = 0.886$  (Wiklind & Combes 1996) and a possible second galaxy at  $z = 0.192$  (Lovell et al. 1996).

Chengalur et al. (1999) first detected HI (and OH) absorption at  $z = 0.886$  in this system using the Westerbork

Synthesis Radio Telescope. Allison et al. (2017) obtained ASKAP spectra of PKS 1830-211 from 700-1530 MHz, re-detecting HI absorption at  $z = 0.192$  and  $z = 0.886$ , and OH absorption at  $z = 0.886$ . Comparing spectra for several epochs spanning 20 years, they identified variability in the HI line, consistent with changes in the background quasar. We include the  $z = 0.886$  HI line detected with ASKAP in our sample here.

## 5 DISCUSSION

### 5.1 HI column density estimates

As noted earlier (§1.3), we need to know both the harmonic mean spin temperature  $T_s$  and the covering factor  $f$  to convert the observed optical depth of a 21 cm HI absorption line to an HI column density  $N_{\text{HI}}$ .

Even without accurate measurements of  $T_s$  and  $f$  for individual sources, however, we can make some general statements about the likely HI column densities along the sightlines where we detected intervening 21 cm absorption lines with ASKAP. In particular, we can consider how many of these detected lines are likely to arise in gas with an HI column density above the DLA threshold of  $2 \times 10^{20} \text{ cm}^{-2}$ . This in turn will allow us to estimate the DLA number density  $n(z)$  in the redshift range probed by our ASKAP spectra.

Since most of the background radio sources in our survey are compact on scales of 100 mas or less (as discussed in §2.3), we will assume for now that the covering factor  $f \sim 1$ . This is a conservative assumption in terms of measuring the total number of DLA systems, since if  $f < 1$ , then the actual HI column density will be higher than that estimated from the observed 21 cm optical depth. We note that the absorber in PKS 1229-02 is likely to have a covering factor  $f < 0.5$  as discussed in section 4.3.

Figure 6 shows how the HI column density  $N_{\text{HI}}$  derived for our four detected lines varies with HI spin temperature. The values plotted assume a covering factor  $f = 1$ , so the derived values of  $N_{\text{HI}}$  will be proportionally higher if  $f < 1$ .

**Table 6.** Parameters of the detected 21 cm absorption lines. The estimated values of  $N_{\text{HI}}$  assume  $T_s = 100$  K and  $f = 1$  (col 6), and equation 9 of Braun 2012 (col 7). Since there can be multiple velocity components in a line, an effective width was determined by dividing the integrated optical depth in this table by the peak value (see e.g. [Dickey 1982](#); [Allison et al. 2013, 2014](#)) - these effective velocity widths are listed in column 8.

Name	$z_{\text{abs}}$	$N_{\text{Gauss}}$	$\tau_{\text{pk}}$	$\int \tau dV$ ( $\text{km.s}^{-1}$ )	Estimated HI column density $N_{\text{HI}}$ ( $\text{cm}^{-2}$ )		Effective width ( $\text{km.s}^{-1}$ )	Notes
(1)	(2)	(3)	(4)	(5)	[ $T_s=100$ K]	[Braun2012]	(8)	(9)
PKS 0834-20	0.5906	3	$0.1596 \pm 0.0051$	$6.178 \pm 0.112$	$1.1 \times 10^{21}$	$1.2 \times 10^{21}$	38.7	ASKAP-12
PKS 1229-02	0.3950	3	$0.0699 \pm 0.0012$	$1.233 \pm 0.021$	$2.2 \times 10^{20}$	$5.3 \times 10^{20}$	17.6	ASKAP-12/36
PKS 1610-77	0.4503	2	$0.0491 \pm 0.0027$	$1.502 \pm 0.058$	$2.7 \times 10^{20}$	$3.7 \times 10^{20}$	30.6	BETA
PKS 1830-211	0.8849	3	$0.0629 \pm 0.0008$	$9.792 \pm 0.050$	$1.8 \times 10^{21}$	$4.8 \times 10^{20}$	155.7	BETA

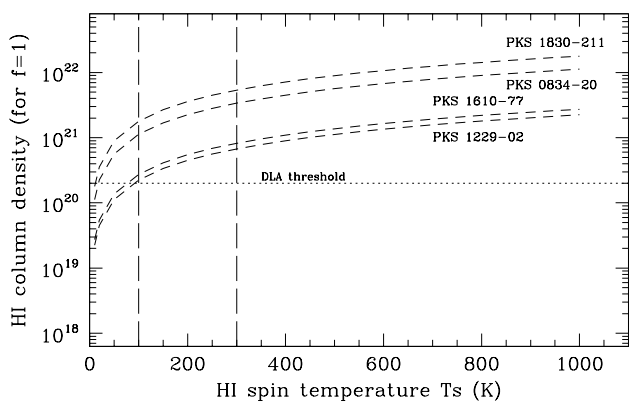


**Figure 6.** HI column densities as a function of assumed spin temperature for the four detected absorption lines presented in §4, derived from the observed optical depth of the line assuming a covering factor  $f = 1$ . Vertical dashed lines at 100 K and 300 K show the approximate range of spin temperatures expected for the cold HI gas detected in absorption with ASKAP (based on the sensitivity plot shown in Figure 3).

We estimate  $N_{\text{HI}}$  from our detected absorption lines in two different ways:

- (i) Taking the commonly-used fiducial value of  $T_s = 100$  K, which assumes all of the absorbing gas is in the CNM ([Wolfire et al. 2003](#)) and so provides a lower limit.
- (ii) Using the empirical relation between  $\tau$  and  $N_{\text{HI}}$  derived by [Braun \(2012\)](#).

The values of  $N_{\text{HI}}$  derived under these two assumptions are listed in columns 6 and 7 of Table 6.

## 5.2 The 21 cm DLA number density at $z \sim 0.6$

In terms of the number of DLA-like absorbers detected in our survey, the results in Table 6 and Figure 6 appear reasonably consistent. Three absorbers (PKS 0834-20, 1610-77 and 1830-211) all have HI column densities above the DLA threshold range both for a range of plausible values of  $T_s$  and  $f$  and for the empirical [Braun \(2012\)](#) relation.

A fourth system, PKS 1229-02, has a 21 cm value closer to the DLA threshold if we assume  $f \sim 1$ , but in this case we also have a direct HST Lyman- $\alpha$  measurement for PKS 1229-

02 of  $N_{\text{HI}} = 5.6 \times 10^{20} \text{ cm}^{-2}$  ([Boissé et al. 1998](#)) which confirms this as a DLA system (see §4.3).

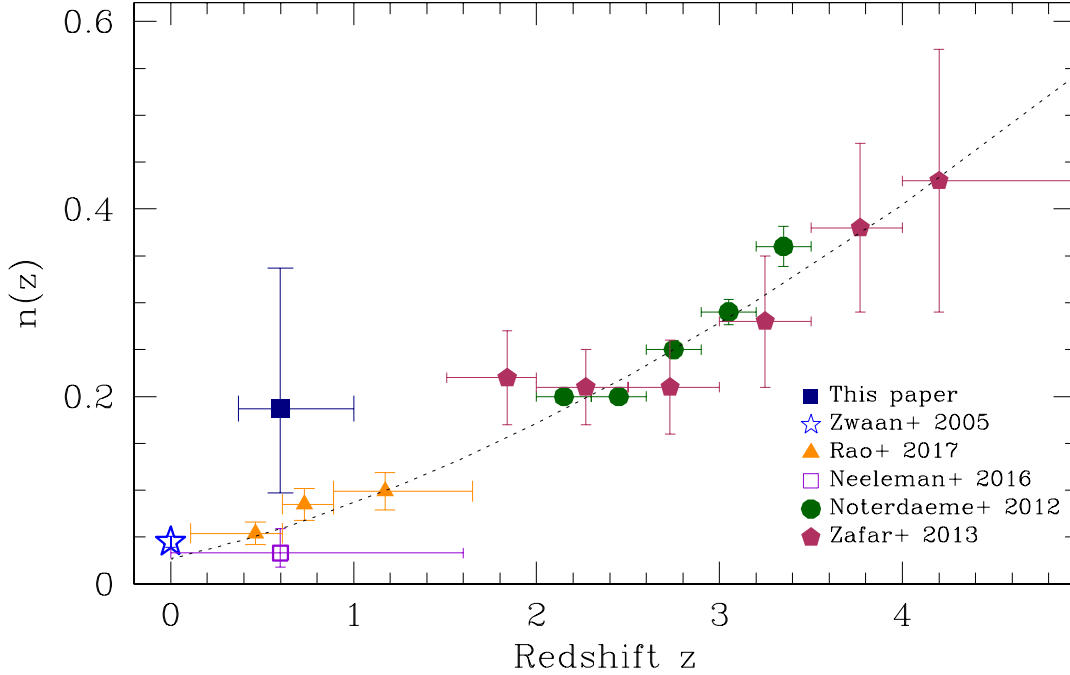
We therefore have four 21 cm DLA detections on sight-lines covering a total redshift interval  $\Delta z = 21.37$ . This yields an estimated DLA number density at redshift  $z \sim 0.6$  of  $dN/dz = 0.19^{+0.15}_{-0.09}$ , where the quoted uncertainties correspond to  $1\sigma$  Gaussian errors calculated for small event numbers ([Gehrels 1986](#)). As can be seen from Figure 3, we are mainly sensitive to gas with a spin temperature typical of the CNM ( $T_s \lesssim 300$  K) and would be unlikely to detect DLA systems arising in warmer gas.

Figure 7 compares our result with those of recent optical DLA studies. The only other 21 cm point is the local ( $z \sim 0$ ) value from [Zwaan et al. \(2005\)](#). The [Neeleman et al. \(2016\)](#) and [Rao et al. \(2017\)](#) values are both from HST observations of damped Ly $\alpha$  lines - the [Rao et al. \(2017\)](#) study preselected targets that showed MgII absorption, while [Neeleman et al. \(2016\)](#) used a smaller HST sample without MgII preselection. The [Noterdaeme et al. \(2012\)](#) study at  $z > 1.7$  used a large ground-based sample of over 6000 SDSS quasars with DLA detections, while [Zafar et al. \(2013\)](#) analyzed a sample of 122 quasar spectra spanning the redshift range  $1.5 < z < 5$ .

It is notable that the ASKAP  $n(z)$  point at  $z \sim 0.6$  lies above the [Neeleman et al. \(2016\)](#) and [Rao et al. \(2017\)](#) values measured at similar redshift, though at this stage the large error bars on the ASKAP value mean that our result is also (just) consistent with the general trend seen in optical DLA studies. Our high value for  $n(z)$  is somewhat surprising, since we are only sensitive to the subset of DLAs with low  $T_s$  - and so our  $n(z)$  value might be expected to be a lower limit to the total value. As can be seen from Figure 6, the HI column densities for our detected absorbers could only lie below the DLA limit if the covering factor  $f = 1$  and the spin temperature dropped below 50–80 K. This appears unlikely, due to the known properties of the CNM and the paucity of observed systems with such low spin temperatures. Figure 7 therefore suggests a potentially significant discrepancy with some of the QSO DLA studies, possibly because we are picking up dusty systems that might not have been included in optical QSO surveys. A larger sample of 21 cm HI absorption detections is needed to explore this question further.

## 5.3 The nature of the intervening galaxies

Since our 21 cm intervening absorbers were selected without any optical pre-selection, identifying their host galaxies gives



**Figure 7.** The number density of DLA absorbers,  $n(z)$ , as a function of redshift. The dark blue square at  $z = 0.6$  shows the 21 cm value derived from our ASKAP pilot survey, as discussed in §5.2 of this paper. The other values plotted are the 21 cm HI emission point from Zwaan et al. (2005), HST DLA values from Neeleman et al. (2016) and Rao et al. (2017), and ground-based DLA measurements from Noterdaeme et al. (2012) and Zafar et al. (2013). The dashed line shows the empirical  $n(z)$  vs  $z$  relation from Rao et al. (2017).

**Table 7.** Spin temperature estimates for the  $z = 0.395$  absorption system towards PKS1229-02, using the  $\text{Ly}\alpha$   $N_{\text{HI}}$  value of  $5.6 \times 10^{20} \text{ cm}^{-2}$  from Boissé et al. (1998)

$T_s$ (K)	Author	Notes
170	Boissé et al. (1998)	Used Brown & Spencer (1979) HI data, which assumes $f = 0.5$
170	Chengalur & Kanekar (2000)	Recomputed from Brown & Spencer (1979) and Briggs (1999) HI data
$105 \pm 30$	Lane (2000)	Used Briggs (1999) HI data
$95 \pm 15$	Kanekar et al. (2014)	Used Brown & Spencer (1979) HI data and $f = 0.42$
$102 \pm 12$	This paper	Using ASKAP HI data, and assuming $f = 0.42$

us a first look at the *kinds* of galaxies that are present in an HI-selected sample in the distant Universe. In contrast to the host galaxies of the high-redshift ( $z > 1.7$ ) DLA systems detected in ground-based optical QSO surveys, the lower-redshift host galaxies of our 21 cm absorbers may be bright enough to detect in high-quality optical images even in the presence of a bright nearby quasar. For example, a typical spiral galaxy at  $z \sim 0.5$  is expected to have an I-band magnitude of 20-22 Cantale et al. (2016) and should be visible in good-quality images from an 8 m-class telescope.

Table 8 summarises the information currently available for the host galaxies of the four HI absorption systems detected in this study, and we discuss each of these absorption systems in turn below.

### 5.3.1 The intervening galaxy group towards PKS 1610-77

The background QSO at  $z = 1.71$  was studied in detail by Courbin et al. (1997), who obtained an R-band optical image

showing three galaxies within a few arcsec of the QSO position. A fourth galaxy was visible in their PSF-subtracted image. Figure 8 shows a schematic view of the positions of the four galaxies found by Courbin et al. (1997), relative to the radio-loud QSO targeted by ASKAP.

Courbin et al. (1997) obtained detailed photometry of the region surrounding the radio-loud QSO, as well as optical spectra of the QSO and a nearby stellar object. They measured R-band magnitudes of 21.3, 21.3, 22.5 and 23.0 respectively for galaxies A, B, C and D, but were uncertain whether these galaxies were associated with PKS 1610-77 itself or foreground objects along the line of sight. They also noted that their QSO spectrum appeared highly reddened in the optical, possibly by absorbing objects along the line of sight.

Courbin et al. (1997) also noted the presence of a strong, unidentified absorption feature at  $8,552\text{\AA}$  in their optical spectrum of PKS 1610-77. We can now identify this feature as  $5895.6\text{\AA}$  NaD absorption at a redshift of  $z = 0.4506$ , i.e.

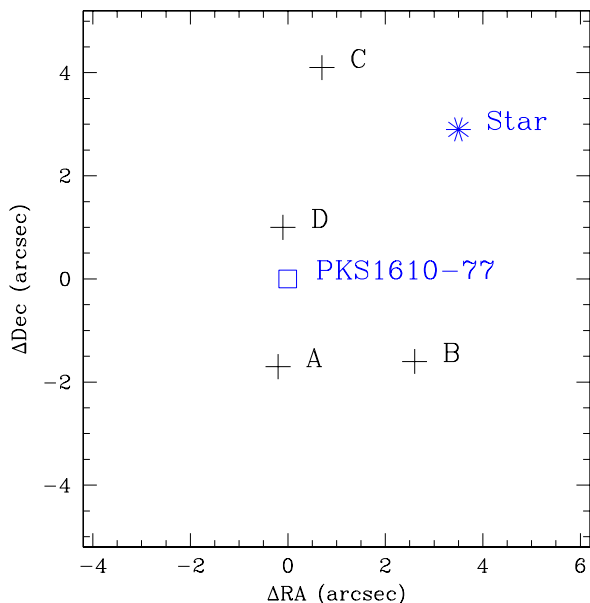


**Figure 8.** Schematic representation of the positions of four galaxies (A, B, C, D) along the line of sight to the radio source PKS 1610-77, based on data from Table 1 of Courbin et al. (1997). The positions of the radio source and a foreground Galactic star are also shown.

the same redshift as the HI absorption line. NaD is a good tracer of cold neutral gas because of its low ionization potential (e.g. Schwartz & Martin 2004), so the identification of this optical line provides independent confirmation of the presence of cold neutral gas at the redshift of our ASKAP HI detection.

In 2018, we obtained optical spectra of the two brightest galaxies in the PKS 1610-77 field (galaxies A and B) with the 8m Gemini-South telescope (see Figure 9). The redshift measured for both these galaxies ( $z = 0.4504$ ) is within  $30 \text{ km s}^{-1}$  of the ASKAP HI absorption redshift ( $z = 0.4503$ ), implying that the intervening HI gas is associated with this galaxy group. At  $z=0.45$ , the impact parameters of galaxies A, B, C and D are 10.0, 17.8, 24.2, and 5.9 kpc respectively. The separation between galaxies A and D is only 2.7 arcsec, corresponding to a projected linear distance of  $\sim 16$  kpc. With no k-correction applied, the approximate R-band absolute magnitudes of the four galaxies are  $-20.7$  (A),  $-20.7$  (B),  $-19.5$  (C) and  $-19.0$  (D).

At this stage, it remains unclear which of the four galaxies in the group is the host galaxy of the HI gas seen in absorption. The spectrum of Galaxy A shows strong NaD absorption, which is absent from the spectrum of Galaxy B, but the spectrum of Galaxy B shows strong  $H\beta$  emission characteristic of ongoing star formation. No spectrum is currently available for Galaxy D, which is the closest to the QSO line of sight, and further observations are needed to resolve this question.

### 5.3.2 The galaxy lens towards PKS 1830-211

This is a well-studied system, though dust extinction (and a density of foreground stars) within the Milky Way means

that optical studies are extremely difficult at the low Galactic latitude of PKS 1830-211 ( $b = -5.7$  deg).

Courbin et al. (2002) and Winn et al. (2002) have identified the lensing galaxy as a face-on spiral, and Koopmans & de Bruyn (2005) showed that the HI absorption could be modelled by an almost face on gaseous disk with a constant rotation velocity and a radially dependent 21-cm optical depth.

Winn et al. (2002) also estimated the lens magnification as a factor  $\sim 5.9$  for the NE component and  $\sim 3.9$  for the SW component of the lensed QSO. PKS 1830-211 is one of the brightest radio sources in our sample. Even if we assume that all the radio emission in this source has been boosted by a factor of six, its unlensed counterpart would still have been bright enough to satisfy the selection criteria in §2.2 of this paper. We therefore retain PKS 1830-211 in our analysis despite the likelihood that its observed radio flux density has been increased by lensing.

### 5.3.3 The intervening system towards PKS 0834-20

We have not yet identified a host galaxy for the HI absorption system at  $z = 0.591$  along the line of sight to PKS 0834-20. A Pan-STARRS (Magnier et al. 2013) image of the field shows faint red objects around 3.6 arcsec west and 4.8 arcsec south-east of the QSO. If these are galaxies at the same redshift at the HI line, the impact parameters would be roughly 25 kpc and 32 kpc respectively. It is currently unclear whether either of these objects is associated with the HI gas seen in absorption.

The only additional information we have at this stage comes from the optical spectrum of the background quasar. The top panel of Figure 10 shows a spectrum of PKS 0834-20 taken in 2018 with the ESO NTT, and the lower panel shows an expanded view of the blue region of this spectrum. Weak metal absorption lines of Fe II and Mg II are seen at a similar redshift to the intervening HI absorption at  $z = 0.591$ .

### 5.3.4 The intervening galaxy towards PKS 1229-02

Steidel et al. (1994) obtained infrared I and K-band images of the PKS 1229-02 field. After subtracting the QSO light, they found two faint objects likely to be foreground galaxies and tentatively identified the  $z = 0.395$  absorption system with a spiral galaxy at an impact parameter of  $\sim 7$  kpc from the background QSO.

This is consistent with the findings of Kronberg et al. (1992), who carried out a detailed multi-frequency analysis of the rotation measure variations along the radio jet in PKS 1229-02. They found that their results were consistent with the presence of an intervening spiral galaxy with an inclination angle of  $\sim 60^\circ$  and an impact parameter of 2 arcsec (around 10 kpc at  $z = 0.395$ ). Hamanowicz et al. (2019, in preparation) have recently observed the PKS 1229-02 field with the MUSE integral-field spectrograph on the ESO VLT. They measure a star-formation rate of  $0.67 \pm 0.09 M_\odot \text{ yr}^{-1}$  for the intervening galaxy, and find that it has sub-solar metallicity (A. Hamanowicz, private communication).

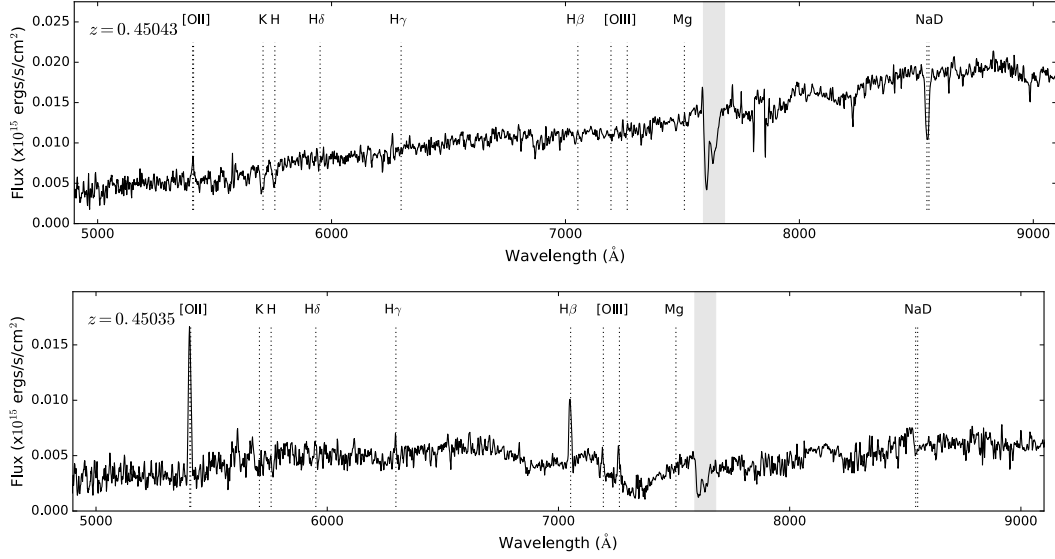


**Figure 9.** Optical spectra of two of the galaxies along the line of sight to PKS 1610-77, taken with the 8 m Gemini-South telescope. (Top) Spectrum of Galaxy A at  $z = 0.45043$ , showing strong NaD absorption. (Bottom) Spectrum of Galaxy B at  $z = 0.45035$ , showing emission lines of H $\beta$ , [OII] and [OIII].

**Table 8.** Potential host galaxies of the intervening HI absorption systems detected in this study

Radio source	$z(\text{HI})$	Potential host	Mag.	Impact parameter	Notes
PKS 0834-20	0.591	Unknown	..	..	No deep optical image available
PKS 1229-02	0.395	Spiral galaxy	..	2 arcsec (11 kpc)	See Briggs et al. (1985); Kronberg et al. (1992)
PKS 1610-77	0.450	Galaxy in group	21.3 (R)	1.7 arcsec (10 kpc)	If galaxy A, see Courbin et al. (1997)
PKS 1830-211	0.886	Spiral galaxy	..	$\ll$ 1 arcsec ( $\ll$ 7 kpc)	See Winn et al. (2002)

## 6 CONCLUSIONS

In this pilot ASKAP study of the sightlines towards 53 bright, compact southern radio sources, we detected four intervening 21 cm HI absorption lines at redshifts ranging from  $z = 0.395$  to  $z = 0.886$ . Two of these (towards PKS 1229-02 and PKS 1830-211) are re-detections of lines from the published literature, and two (towards PKS 0834-20 and PKS 1610-77) are detected here for the first time.

We used these detections to make a new estimate of the DLA number density at redshift  $z \sim 0.6$ ,  $n(z) = 0.19^{+0.15}_{-0.09}$ . This value lies above the general trend seen in optical and ultraviolet studies of QSO DLA systems (e.g. Rao et al. 2017; Zafar et al. 2013; Noterdaeme et al. 2012), as can be seen from Figure 7.

From the small sample observed here, it appears that our detected HI absorption lines arise mainly in the disks of spiral or late-type galaxies, with impact parameters typically less than 10–15 kpc. At least one of the background radio-loud QSOs (PKS 1610-77) is highly reddened (presumably by the intervening galaxy group identified by Courbin et al. (1997) and detected here in HI) and would probably not have been selected in an optical QSO survey.

Our pilot results are encouraging for two reasons. Firstly, the redshift interval covered by a single ASKAP spectrum,  $\Delta z \sim 0.6$ , is large enough to carry out spectroscopically untargeted 21 cm searches for intervening HI absorp-

tion systems - a significant advance over earlier radio studies (e.g. Lane et al. 1998) where optical preselection (often based on the Mg II absorption line) was required. Secondly, the 700-1000 MHz ASKAP band is free from terrestrial radio interference (in contrast to the case at most major radio observatories around the world), meaning that the full redshift interval can be searched for 21 cm absorption lines.

While this pilot survey has focused on observations of individual bright radio sources, the completed 36-antenna ASKAP telescope will have sufficient sensitivity to search for HI absorption simultaneously on sightlines to over 100 radio sources across a  $30 \text{ deg}^2$  field of view (Johnston et al. 2008). The full all-sky FLASH dataset will cover a total redshift path length  $\Delta z \sim 50,000$ . This opens up the exciting possibility of detecting several hundred new 21 cm absorption systems out to  $z \sim 1$ , allowing us to improve our knowledge of the amount and physical state of neutral hydrogen in individual galaxies in the distant Universe.

## DATA AVAILABILITY

The data underlying this article will be shared on reasonable request to the corresponding author.

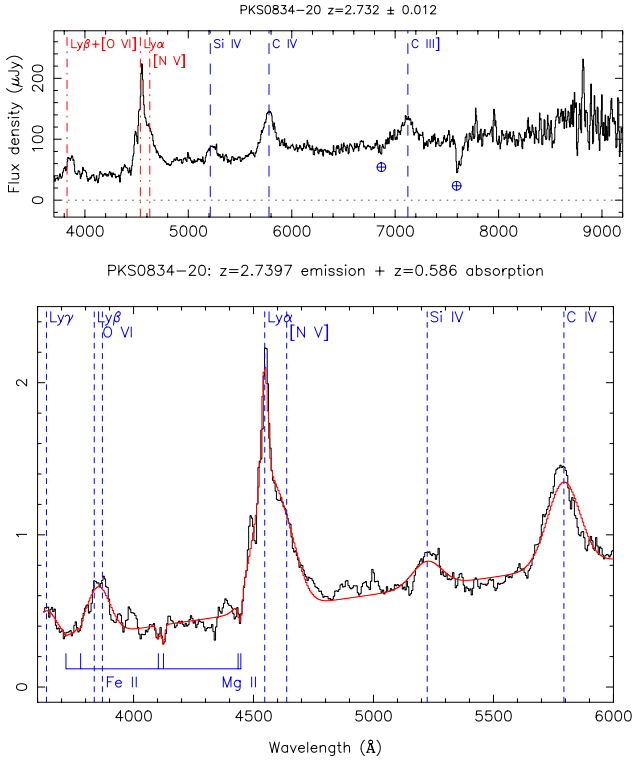


**Figure 10.** (Top) Optical spectrum of the quasar PKS0834-20, taken with the 3.5m ESO NTT in March 2018, with the main spectral lines labelled. (Bottom) Close-up of the region blueward of Ly $\alpha$ , showing metal absorption lines of FeII and MgII at  $z = 0.586$ , close to the 21 cm HI absorption redshift of  $z = 0.591$ .

## ACKNOWLEDGEMENTS

We acknowledge the financial support of the Australian Research Council through grant CE170100013 (ASTRO 3D). The initial stages of this research were supported by the Australian Research Council Centre of Excellence for All Sky Astrophysics (CAASTRO), through grant CE110001020.

The Australian SKA Pathfinder is part of the Australia Telescope National Facility which is managed by CSIRO. Operation of ASKAP is funded by the Australian Government with support from the National Collaborative Research Infrastructure Strategy. ASKAP uses the resources of the Pawsey Supercomputing Centre. Establishment of ASKAP, the Murchison Radio-astronomy Observatory and the Pawsey Supercomputing Centre are initiatives of the Australian Government, with support from the Government of Western Australia and the Science and Industry Endowment Fund. We acknowledge the Wajarri Yamatji people as the traditional owners of the Observatory site.

We gratefully acknowledge and thank the ASKAP commissioning team for the use of BETA and ASKAP-12 during the commissioning phase, which allowed us to carry out the observations described in this paper.

Based on observations collected at the European Southern Observatory under ESO program 0100.A-0588(A).

Based on observations obtained under program ID GS-2017B-Q-63 at the Gemini Observatory which is operated by the Association of Universities for Research in Astronomy,

Inc., under a cooperative agreement with the NSF on behalf of the Gemini partnership: the National Science Foundation (United States), National Research Council (Canada), CONICYT (Chile), Ministerio de Ciencia, Tecnología e Innovación Productiva (Argentina), Ministério da Ciência, Tecnologia e Inovação (Brazil), and Korea Astronomy and Space Science Institute (Republic of Korea).

This research has made use of the NASA/IPAC Extragalactic Database (NED), which is operated by the Jet Propulsion Laboratory, California Institute of Technology, under contract with the National Aeronautics and Space Administration.

We thank Céline Péroux for helpful comments on an earlier draft of this paper, and Filippo Maccagni for carrying out one of the ESO NTT observing runs.

EMS, VAM and JRA also thank the Munich Institute for Astro- and Particle Physics (MIAPP) for supporting our attendance at the 2019 MIAPP program on ‘Galaxy Evolution in a New Era of HI Surveys’, which provided a stimulating venue for discussions and allowed us to complete this paper.

## REFERENCES

- Allison J. R., Sadler E. M., Whiting M. T., 2012, *Publ. Astron. Soc. Australia*, **29**, 221
- Allison J. R., Curran S. J., Sadler E. M., Reeves S. N., 2013, *MNRAS*, **430**, 157
- Allison J. R., Sadler E. M., Meekin A. M., 2014, *MNRAS*, **440**, 696
- Allison J. R., et al., 2015, *MNRAS*, **453**, 1249
- Allison J. R., et al., 2017, *MNRAS*, **465**, 4450
- Allison J. R., et al., 2019, *MNRAS*, **482**, 2934
- Allison J. R., et al., 2020, *MNRAS*, **494**, 3627
- Arp H. C., Bolton J. G., Kinman T. D., 1967, *ApJ*, **147**, 840
- Beasley A. J., Gordon D., Peck A. B., Petrov L., MacMillan D. S., Fomalont E. B., Ma C., 2002, *ApJS*, **141**, 13
- Berg T. A. M., et al., 2017, *MNRAS*, **464**, L56
- Boissé P., Le Brun V., Bergeron J., Deharveng J.-M., 1998, *A&A*, **333**, 841
- Braun R., 2012, *ApJ*, **749**, 87
- Briggs F. H., 1999, in Carilli C. L., Radford S. J. E., Menten K. M., Langston G. I., eds, *Astronomical Society of the Pacific Conference Series Vol. 156, Highly Redshifted Radio Lines*. p. 16 ([arXiv:astro-ph/9806182](https://arxiv.org/abs/astro-ph/9806182))
- Briggs F. H., Wolfe A. M., 1983, *ApJ*, **268**, 76
- Briggs F. H., Turnshek D. A., Schaeffer J., Wolfe A. M., 1985, *ApJ*, **293**, 387
- Brown R. L., Mitchell K. J., 1983, *ApJ*, **264**, 87
- Brown R. L., Roberts M. S., 1973, *ApJ*, **184**, L7
- Brown R. L., Spencer R. E., 1979, *ApJ*, **230**, L1
- Callingham J. R., et al., 2017, *ApJ*, **836**, 174
- Cantale N., et al., 2016, *A&A*, **589**, A82
- Chen H.-W., Lanzetta K. M., 2003, *ApJ*, **597**, 706
- Chen H.-W., Boettcher E., Johnson S. D., Zahedy F. S., Rudie G. C., Cooksey K. L., Rauch M., Mulchaey J. S., 2019, *ApJ*, **878**, L33
- Chengalur J. N., Kanekar N., 2000, *MNRAS*, **318**, 303
- Chengalur J. N., de Bruyn A. G., Narasimha D., 1999, *A&A*, **343**, L79
- Chhetri R., Ekers R. D., Jones P. A., Ricci R., 2013, *MNRAS*, **434**, 956
- Chippendale A. P., et al., 2015, in 2015 International Conference on Electromagnetics in Advanced Applications

- (ICEAA), p. 541-544. pp 541-544 ([arXiv:1509.00544](https://arxiv.org/abs/1509.00544)), [doi:10.1109/ICEAA.2015.7297174](https://doi.org/10.1109/ICEAA.2015.7297174)
- Condon J. J., Cotton W. D., Greisen E. W., Yin Q. F., Perley R. A., Taylor G. B., Broderick J. J., 1998, *AJ*, **115**, 1693
- Courbin F., Hutsemekers D., Meylan G., Magain P., Djorgovski S. G., 1997, *A&A*, **317**, 656
- Courbin F., Meylan G., Kneib J.-P., Lidman C., 2002, *ApJ*, **575**, 95
- D'Ammando F., et al., 2012, *MNRAS*, **427**, 893
- Darling J., Giovanelli R., Haynes M. P., Bolatto A. D., Bower G. C., 2004, *ApJ*, **613**, L101
- Davé R., Katz N., Oppenheimer B. D., Kollmeier J. A., Weinberg D. H., 2013, *MNRAS*, **434**, 2645
- DeBoer D. R., et al., 2009, *IEEE Proceedings*, **97**, 1507
- Delhaize J., Meyer M. J., Staveley-Smith L., Boyle B. J., 2013, *MNRAS*, **433**, 1398
- Dickey J. M., 1982, *ApJ*, **263**, 87
- Diemer B., et al., 2019, *MNRAS*, **487**, 1529
- Drinkwater M. J., et al., 1997, *MNRAS*, **284**, 85
- Ellison S. L., 2006, *MNRAS*, **368**, 335
- Ellison S. L., Hall P. B., Lira P., 2005, *AJ*, **130**, 1345
- Ellison S. L., Kanekar N., Prochaska J. X., Momjian E., Worseck G., 2012, *MNRAS*, **424**, 293
- Fall S. M., Pei Y. C., 1989, *ApJ*, **337**, 7
- Fey A. L., et al., 2015, *AJ*, **150**, 58
- Fomalont E. B., Frey S., Paragi Z., Gurvits L. I., Scott W. K., Taylor A. R., Edwards P. G., Hirabayashi H., 2000, *ApJS*, **131**, 95
- Fomalont E. B., Petrov L., MacMillan D. S., Gordon D., Ma C., 2003, *AJ*, **126**, 2562
- Fricke K. J., Kollatschny W., Witzel A., 1983, *A&A*, **117**, 60
- Gehrels N., 1986, *ApJ*, **303**, 336
- Geier S. J., et al., 2019, *A&A*, **625**, L9
- Glowacki M., et al., 2019, *MNRAS*, **489**, 4926
- Halpern J. P., Eracleous M., Mattox J. R., 2003, *AJ*, **125**, 572
- Healey S. E., et al., 2008, *ApJS*, **175**, 97
- Heintz K. E., et al., 2018, *A&A*, **615**, A43
- Hewett P. C., Wild V., 2010, *MNRAS*, **405**, 2302
- Heywood I., et al., 2016, *MNRAS*, **457**, 4160
- Hintzen P., Ulvestad J., Owen F., 1983, *AJ*, **88**, 709
- Horiuchi S., et al., 2004, *ApJ*, **616**, 110
- Hotan A. W., et al., 2014, *Publ. Astron. Soc. Australia*, **31**, e041
- Hunstead R. W., Murdoch H. S., 1980, *MNRAS*, **192**, 31P
- Hunstead R. W., Murdoch H. S., Shobbrook R. R., 1978, *MNRAS*, **185**, 149
- Hunt L. R., Pisano D. J., Edell S., 2016, *AJ*, **152**, 30
- Jackson C. A., Wall J. V., Shaver P. A., Kellermann K. I., Hook I. M., Hawkins M. R. S., 2002, *A&A*, **386**, 97
- Jauncey D. L., et al., 1991, *Nature*, **352**, 132
- Johnston S., et al., 2008, *Experimental Astronomy*, **22**, 151
- Jones D. H., et al., 2009, *MNRAS*, **399**, 683
- Kanekar N., Briggs F. H., 2004, *New Astron. Rev.*, **48**, 1259
- Kanekar N., Prochaska J. X., Ellison S. L., Chengalur J. N., 2009, *MNRAS*, **396**, 385
- Kanekar N., et al., 2014, *MNRAS*, **438**, 2131
- Kanekar N., Sethi S., Dwarakanath K. S., 2016, *ApJ*, **818**, L28
- Kinman T. D., Burbidge E. M., 1967, *ApJ*, **148**, L59
- Koopmans L. V. E., de Bruyn A. G., 2005, *MNRAS*, **360**, L6
- Krogager J.-K., Fynbo J. P. U., Møller P., Noterdaeme P., Heintz K. E., Pettini M., 2019, *MNRAS*, **486**, 4377
- Kronberg P. P., Perry J. J., Zukowski E. L. H., 1992, *ApJ*, **387**, 528
- Lagos C. D. P., Baugh C. M., Zwaan M. A., Lacey C. G., Gonzalez-Perez V., Power C., Swinbank A. M., van Kampen E., 2014, *MNRAS*, **440**, 920
- Lagos C. d. P., Tobar R. J., Robotham A. S. G., Obreschkow D., Mitchell P. D., Power C., Elahi P. J., 2018, *MNRAS*, **481**, 3573
- Lah P., et al., 2007, *MNRAS*, **376**, 1357
- Lane W. M., 2000, PhD thesis, University of Groningen
- Lane W., Smette A., Briggs F., Rao S., Turnshek D., Meylan G., 1998, *AJ*, **116**, 26
- Lanzetta K. M., Bowen D. V., 1992, *ApJ*, **391**, 48
- Lanzetta K. M., Wolfe A. M., Turnshek D. A., 1995, *ApJ*, **440**, 435
- Liang E. W., Liu H. T., 2003, *MNRAS*, **340**, 632
- Lidman C., Courbin F., Meylan G., Broadhurst T., Frye B., Welch W. J. W., 1999, *ApJ*, **514**, L57
- Lovell J. E. J., et al., 1996, *ApJ*, **472**, L5
- Ma C., et al., 1998, *AJ*, **116**, 516
- Magnier E. A., et al., 2013, *ApJS*, **205**, 20
- Marshall H. L., et al., 2005, *ApJS*, **156**, 13
- Marshall H. L., et al., 2011, *ApJS*, **193**, 15
- Marziani P., Sulentic J. W., Dultzin-Hacyan D., Calvani M., Moles M., 1996, *ApJS*, **104**, 37
- Massardi M., et al., 2008, *MNRAS*, **384**, 775
- Mauch T., Murphy T., Buttery H. J., Curran J., Hunstead R. W., Piestrzynski B., Robertson J. G., Sadler E. M., 2003, *MNRAS*, **342**, 1117
- McConnell D., Sadler E. M., Murphy T., Ekers R. D., 2012, *MNRAS*, **422**, 1527
- McConnell D., et al., 2016, *Publ. Astron. Soc. Australia*, **33**, e042
- McMullin J. P., Waters B., Schiebel D., Young W., Golap K., 2007, in Shaw R. A., Hill F., Bell D. J., eds, *Astronomical Society of the Pacific Conference Series Vol. 376, Astronomical Data Analysis Software and Systems XVI*. p. 127
- Morganti R., Oosterloo T., 2018, *A&ARv*, **26**, 4
- Morganti R., Sadler E. M., Curran S., 2015, *Advancing Astrophysics with the Square Kilometre Array (ASKA14)*, p. 134
- Morton D. C., Tritton K. P., 1982, *MNRAS*, **198**, 669
- Morton D. C., Savage A., Bolton J. G., 1978, *MNRAS*, **185**, 735
- Moss V. A., et al., 2017, *MNRAS*, **471**, 2952
- Murdoch H. S., Hunstead R. W., White G. L., 1984, *Proceedings of the Astronomical Society of Australia*, **5**, 341
- Murphy T., Mauch T., Green A., Hunstead R. W., Piestrzynska B., Kels A. P., Sztajer P., 2007, *MNRAS*, **382**, 382
- Murphy T., et al., 2010, *MNRAS*, **402**, 2403
- Murray C. E., Stanimirović S., Goss W. M., Heiles C., Dickey J. M., Babler B., Kim C.-G., 2018, *ApJS*, **238**, 14
- Neeleman M., Prochaska J. X., Ribaudo J., Lehner N., Howk J. C., Rafelski M., Kanekar N., 2016, *ApJ*, **818**, 113
- Noterdaeme P., et al., 2012, *A&A*, **547**, L1
- O'Dea C. P., Baum S. A., Stanghellini C., 1991, *ApJ*, **380**, 66
- Ojha R., et al., 2005, *AJ*, **130**, 2529
- Ojha R., et al., 2010, *A&A*, **519**, A45
- Osmer P. S., Porter A. C., Green R. F., 1994, *ApJ*, **436**, 678
- Péroux C., et al., 2019, *MNRAS*, **485**, 1595
- Peterson B. A., Jauncey D. L., Condon J. J., Wright A. E., 1976, *ApJ*, **207**, L5
- Peterson B. A., Wright A. E., Jauncey D. L., Condon J. J., 1979, *ApJ*, **232**, 400
- Petrov L., Phillips C., Bertarini A., Murphy T., Sadler E. M., 2011, *MNRAS*, **414**, 2528
- Petrov L., de Witt A., Sadler E. M., Phillips C., Horiuchi S., 2019, *MNRAS*, **485**, 88
- Pontzen A., Pettini M., 2009, *MNRAS*, **393**, 557
- Pushkarev A. B., Kovalev Y. Y., Lister M. L., Savolainen T., 2017, *MNRAS*, **468**, 4992
- Rao S. M., Turnshek D. A., 2000, *ApJS*, **130**, 1
- Rao S. M., Turnshek D. A., Nestor D. B., 2006, *ApJ*, **636**, 610
- Rao S. M., Turnshek D. A., Sardane G. M., Monier E. M., 2017, *MNRAS*, **471**, 3428
- Reynolds J., 1994, *A Revised Flux Scale for the AT Compact Array*, Unpublished technical memo available at <http://www.atnf.csiro.au/observers/memos/d96783~1.pdf>
- Saikia D. J., Shastri P., Cornwell T. J., Junor W., Muxlow

- T. W. B., 1989, *Journal of Astrophysics and Astronomy*, **10**, 203
- Sambruna R. M., Gambill J. K., Maraschi L., Tavecchio F., Cerutti R., Cheung C. C., Urry C. M., Chartas G., 2004, *ApJ*, **608**, 698
- Sault R. J., Teuben P. J., Wright M. C. H., 1995, in Shaw R. A., Payne H. E., Hayes J. J. E., eds, *Astronomical Society of the Pacific Conference Series Vol. 77, Astronomical Data Analysis Software and Systems IV*. p. 433 ([arXiv:astro-ph/0612759](https://arxiv.org/abs/astro-ph/0612759))
- Savage A., Wright A. E., 1981, *MNRAS*, **196**, 927
- Schwartz C. M., Martin C. L., 2004, *ApJ*, **610**, 201
- Serra P., et al., 2015, *MNRAS*, **452**, 2680
- Shaw M. S., et al., 2012, *ApJ*, **748**, 49
- Steidel C. C., Pettini M., Dickinson M., Persson S. E., 1994, *AJ*, **108**, 2046
- Stickel M., Fried J. W., Kuehr H., 1989, *A&AS*, **80**, 103
- Strittmatter P. A., Carswell R. F., Gilbert G., Burbidge E. M., 1974, *ApJ*, **190**, 509
- Subrahmanyan R., Narasimha D., Pramesh-Rao A., Swarup G., 1990, *MNRAS*, **246**, 263
- Tadhunter C. N., Morganti R., di Serego-Alighieri S., Fosbury R. A. E., Danziger I. J., 1993, *MNRAS*, **263**, 999
- Thompson D. J., Djorgovski S., de Carvalho R., 1990, *PASP*, **102**, 1235
- Titov O., Stanford L. M., Johnston H. M., Pursimo T., Hunstead R. W., Jauncey D. L., Maslennikov K., Boldycheva A., 2013, *AJ*, **146**, 10
- Turnshek D. A., Rao S. M., 2002, *ApJ*, **572**, L7
- White G. L., Jauncey D. L., Wright A. E., Batty M. J., Savage A., Peterson B. A., Gulkis S., 1988, *ApJ*, **327**, 561
- Wiklund T., Combes F., 1996, *Nature*, **379**, 139
- Wilkes B. J., 1986, *MNRAS*, **218**, 331
- Wilkes B. J., Wright A. E., Jauncey D. L., Peterson B. A., 1983, *Proceedings of the Astronomical Society of Australia*, **5**, 2
- Winn J. N., Kochanek C. S., McLeod B. A., Falco E. E., Impey C. D., Rix H.-W., 2002, *ApJ*, **575**, 103
- Wisotzki L., Christlieb N., Bade N., Beckmann V., Köhler T., Vanelle C., Reimers D., 2000, *A&A*, **358**, 77
- Wolfe A. M., 1980, *Phys. Scr.*, **21**, 744
- Wolfe A. M., Turnshek D. A., Smith H. E., Cohen R. D., 1986, *ApJS*, **61**, 249
- Wolfe A. M., Gawiser E., Prochaska J. X., 2005, *ARA&A*, **43**, 861
- Wolfire M. G., McKee C. F., Hollenbach D., Tielens A. G. G. M., 2003, *ApJ*, **587**, 278
- Wright A. E., Jauncey D. L., Peterson B. A., Condon J. J., 1977, *ApJ*, **211**, L115
- Wright A. E., Ables J. G., Allen D. A., 1983, *MNRAS*, **205**, 793
- Zafar T., Péroux C., Popping A., Milliard B., Deharveng J.-M., Frank S., 2013, *A&A*, **556**, A141
- Zwaan M. A., van der Hulst J. M., Briggs F. H., Verheijen M. A. W., Ryan-Weber E. V., 2005, *MNRAS*, **364**, 1467
- Zwaan M. A., Liske J., Péroux C., Murphy M. T., Bouché N., Curran S. J., Biggs A. D., 2015, *MNRAS*, **453**, 1268
- di Serego-Alighieri S., Danziger I. J., Morganti R., Tadhunter C. N., 1994, *MNRAS*, **269**, 998
- van de Voort F., Schaye J., Altay G., Theuns T., 2012, *MNRAS*, **421**, 2809

## APPENDIX A: NOTES ON INDIVIDUAL SOURCES

**PKS 0903-57:** This source is at low Galactic latitude ( $b = -7.0$  deg). [Thompson et al. \(1990\)](#) quote a redshift of  $z=0.695\pm 0.003$ , based on lines of redshifted MgII 2798 seen at  $4751 \text{ \AA}$  and [OII] 3727 at  $6306 \text{ \AA}$ , but the spectrum shown in their paper is noisy and the lines appear very weak. It

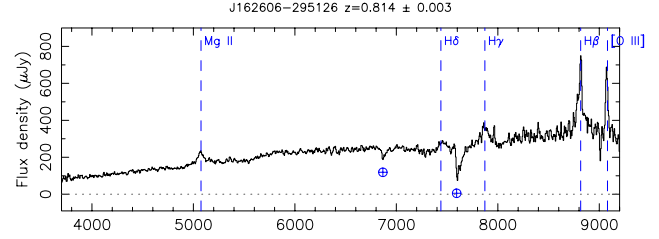


**Figure A1.** Optical spectrum of the radio source PKS 1622-29, taken with the 3.5m ESO NTT in March 2018, with the main spectral lines labelled.

also remains unclear whether the object observed is the correct optical ID for the radio source. We therefore regard the redshift of PKS 0903-57 as uncertain at present.

**MRC 1039-474:** The J2000 ICRF position listed by [Ma et al. \(1998\)](#) (10:41:42.940 -47:40:06.53) is offset by about 18 arcsec from the VLBI position listed by [Titov et al. \(2013\)](#) (10:41:44.650 -47:40:00.06). We adopt the [Titov et al. \(2013\)](#) position, which is consistent with both the AT20G position listed by [Murphy et al. \(2010\)](#) and the optical position of the background QSO.

**PKS 1127-14** An intervening 21 cm HI absorption line at  $z = 0.313$  was detected by [Lane et al. \(1998\)](#) and [Chengalur & Kanekar \(2000\)](#). This line is outside the redshift range covered by the ASKAP observations in Tables 1 and 2, but has recently been studied in detail by [Péroux et al. \(2019\)](#) and [Chen et al. \(2019\)](#).

**PKS 1622-29:** A redshift of  $z=0.815$  is listed in the 1990 PKS catalogue, and is quoted in several published papers. As noted by [Jackson et al. \(2002\)](#) however, the initial redshift measurement cannot be traced back to any published source. A new spectrum taken with the ESO NTT in 2018 and reproduced in Figure A1, gives a redshift of  $z = 0.814$ , and so confirms the original literature redshift.

**PKS 1740-571:** This source has a 21 cm HI absorption line at  $z = 0.441$  identified as an associated absorption system by [Allison et al. \(2015\)](#).

**MRC 1759-396:** NED lists a possible redshift of  $z=0.293$  ([Liang & Liu 2003](#)), but we were unable to trace this back to its original source. Instead, we adopt the redshift of  $z=1.319$  measured by [Shaw et al. \(2012\)](#) from an ESO NTT spectrum.

**PKS 2123-463:** [Jackson et al. \(2002\)](#) note that the early redshift measurements by [Savage & Wright \(1981\)](#), based on objective-prism spectra, is not reliable and so the redshift of this object remains unknown. [D’Ammando et al. \(2012\)](#) estimate a photometric redshift of  $z \sim 1.46$  based on SED fitting.

**PKS 2223-05:** NED lists a  $z = 0.4842$  QSO DLA system found by [Lanzetta et al. \(1995\)](#) in IUE spectra. No published HST spectrum is available to confirm this detection, and

Turnshek & Rao (2002) note that the lack of MgII and FeII absorption lines at this redshift makes it unlikely that this  $z = 0.4842$  system is a genuine DLA. Chengalur & Kanekar (2000) failed to detect 21 cm absorption at  $z = 0.484$ , and we also see no absorption at this redshift in our ASKAP spectrum.

This paper has been typeset from a  $\text{\TeX/L}^{\text{A}}\text{\TeX}$  file prepared by the author.